Borehole-Breathing/Kick Discriminator: Diagnostic Tool and Potential Resource for In-Situ Formation Characterization

S. Baldino, S. Z. Miska, and **E. M. Ozbayoglu,** University of Tulsa, and **J. Zhang,** BP

Summary

In most drilling environments, wellbore pressure exceeding the fracture-opening/initiation gradient often results in major fluid losses when drilling ahead and fluid returns when circulation is stopped. The phenomenon is generally referred to as wellbore breathing. Because no flow is expected when circulation is stopped, the mudflow return is more noticeable and could lead to kick misdiagnosis. To rapidly identify whether a possible influx is caused by formation breathing (or otherwise), correct interpretation and modeling of this phenomenon are paramount. The latter can be used to generate a reliable diagnostic tool for breathing discrimination, and it can also be turned into a valuable resource. Potentially, several in-situ properties of the fractured formation can be inferred with static flowback signatures and pressure-while-drilling (PWD) data. This paper shows how to use the proposed geomechanical model to generate diagnostic flowback type curves. A step-by-step procedure is then presented to discriminate the nature of the influx and to infer the fracture-network properties (damaged radius, generalized hydraulic diffusivity, average borehole breathability, and generalized total compressibility) through a type-curve matching protocol. Several field data have been analyzed to show the applicability of the proposed diagnostic tool and to validate its ability to rapidly differentiate borehole breathing from a kick.

Introduction

Drilling operations are becoming more challenging every day as high-temperature/high-pressure and deepwater wells are targeted. One of the primary concerns of these types of drilling environments is the narrow margin between the pore pressure and fracture-opening/initiation gradient. Because of the pressure fluctuations taking place in the wellbore as a result of intermittent circulation of drilling mud, sizable drilling-fluid-loss/gain events might occur. This is particularly true when a fracture network of limited length intercepts the well. The phenomenon is generally referred to as wellbore ballooning or breathing. Accordingly, borehole breathing is the term used in this work to address reversible mud losses in fractured formations. Originally, the radial expansion and contraction of tubular elements (riser, casing, and open hole) because of pressure variations in the wellbore have been addressed as the main cause behind breathing (Gill 1989; Helstrup et al. 2001). Compressibility effects and thermal volumetric changes of drilling fluids have also been investigated as causes leading to breathing events (Karstad 1998; Babu 1998; Aadnøy 2010; Yuan et al. 2016). Nonetheless, it is widely recognized that hydraulic communication between the borehole and fractures represents the main source of breathing (Tare et al. 2001; Lavrov and Tronvoll 2005; Ozdemirtas et al. 2009). The latter is commonly observed under different situations. Among them, there is drilling through zones characterized by a *limited* fracture network with negligible leakoff into the surrounding formation and drilling in deepwater environments with a narrow operating window between the pore pressure and fracture gradient (Ward and Clark 1998; Tare et al. 2001; Erivwo and Adeleye 2012). The fluid progressively flows in and out of the fractures as a consequence of three mechanisms: (1) bulk volume deformation, (2) fluid compressibility, and (3) fracture-aperture variation. The latter is a direct consequence of fracture pressure buildup and drawdown caused by wellbore pressure fluctuations. More specifically, during circulation, the borehole is exposed to the equivalent circulating density (ECD). The ECD corresponds to the equivalent static density (ESD) plus the additional contribution coming from the frictional pressure losses caused by drilling fluid flowing in the annulus. If the resulting bottomhole pressure increases over the fracture-opening/initiation gradient, drilling fluid will migrate into the hydraulically connected fractures intercepting the well. As soon as circulation is stopped, the bottomhole pressure decreases and causes the fractures to partially close. This occurs during a pumps-off period (connection, tripping or flow check operations) and might cause a significant amount of mud to be returned into the wellbore. The mud-flow return occurs at a rapid rate, and because no flow is expected to occur during pumps-off periods, it is therefore more noticeable **(Fig. 1).** Kick misdiagnosis represents one of the most dangerous consequences of wellbore-breathing misinterpretation. This happens if the measured return flow is wrongly interpreted as a kick (and vice versa) when the pumps are shut down (Baldino et al. 2018). It follows that the major issue related to borehole breathing is to recognize this problem correctly and not to confuse it with reservoir influxes and other lost-circulation events. If borehole breathing is correctly identified, the most practical steps to contain it can be followed in the field (Power et al. 2003). Given this pattern, it is not surprising that breathing is considered a safety issue by so many field engineers and rig crews. Even among those who develop advanced kick-detection techniques (Fraser et al. 2014; Johnson et al. 2014; Tarr et al. 2016; Samuel 2018), the occurrence of breathing must surely be seen as potentially problematic. Whether wellbore breathing must be seen universally as a problem, though, is open to question. This point will be raised again in the next section.

Motivation

Most reports of breathing in fractured formations focus on a particular wellbore or mitigation approach, rather than tackling the global process; thus, there are far more presentations of breathing events than there are comparisons (Ashley 2000; Rosenberg and Gala 2011; Tirado Vargas et al. 2011; Golwalkar et al. 2016). Some of those authors do make comparisons of two or three cases of breathing but desist from further generalization. This situation, indeed, is no more than characteristic of industrial publications, which have always been overwhelmingly particularistic. Nonetheless, a remarkable effort has been put into using real-time data to analyze borehole breathing (Ward and Clark 1998; Dalton et al. 2002). However, hundreds of formation-exposure hours might be necessary to identify the fractures through image logs (Dalton et al. 2002). The goal of this study throughout is to look at breathing in fractured formations as a

Original SPE manuscript received for review 18 December 2018. Revised manuscript received for review 9 March 2019. Paper (SPE 195689) peer approved 12 March 2019.

general phenomenon to gain an understanding not limited to specific cases, but applicable across different types of drilling environments. In this work, the concept of type curves is used to provide the engineers with the most general breathing discriminator. It focuses on the unique signature that breathing displays during the flowback phase, with the scope to generate a far-reaching tool applicable to any type of wellbore and/or formation. Considering the flowback phase also makes the resulting type curves equally applicable to natural and/or drilling-induced fractures. In fact, regardless of their origin, fractures are already present and charged, waiting only to be depleted as the wellbore pressure declines. One additional outcome of such an approach is that breathing can also be turned from a problem into a valuable resource. When dealing with natural or drilling-induced fractures, the knowledge of their properties can have a significant technical and economic impact. If natural fractures are involved, production and reservoir-management strategies can benefit from an in-situ fracture-network description (Segatto and Colombo 2011; Gale et al. 2014; Mi et al. 2016). Moreover, the presence of natural fractures could alter the propagating direction of hydraulic fractures, fracture width, and stress field in terms of geomechanical effects. The latter largely relies on natural-fracture intensity orientation, the principal stress directions, and the strength of fracture planes (Zhou et al. 2015; Jamison and Azad 2017). On the other hand, wellbore-stability analysis could significantly benefit from a characterization of natural and/or drilling-induced fractures (Meng et al. 2019). As a reversible mud loss, breathing can be effectively used as a tool to identify and characterize the fractured formation in the near-wellbore region.

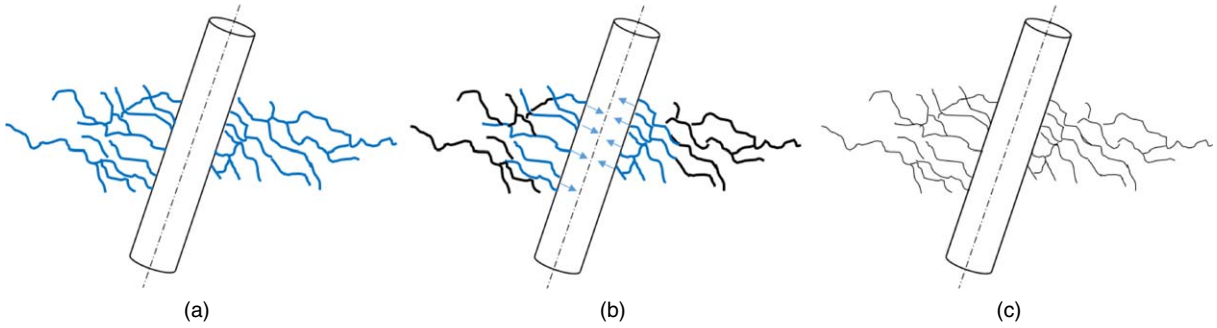

Fig. 1—Sequence of mud-flow return to the well: (a) fractures are charged; (b) depletion starts; and (c) fractures are depleted and closed.

Fracture Characterization

In the literature, an extensive effort has been made to model the mechanism of fluid invasion into natural and/or induced fractures. As a result, important insights could be obtained regarding fracture properties such as the aperture, hydraulic conductivity, and effective volume. Some authors focused on drilling-fluid total losses. Among them, Liétard et al. (1996) derived curves for mud invasion vs. time for different hydraulic apertures on the basis of numerical solutions of the governing equations. Subsequently, Liétard et al. (1999) refined this work, presenting mud-loss-volume vs. time type curves for the estimation of the fracture aperture by means of curve matching. Majidi et al. (2010) proposed a protocol, on the basis of type-curve matching, that quantitatively analyzed mud total losses. The model accounts for fluid rheology (yield power law) and allows for hydraulic aperture estimation. More recently, Huang et al. (2011) reviewed the work of Liétard et al. (1999) and presented a more direct and straightforward method to infer the hydraulic-fracture width on the basis of the solution of the cubic equation. Another rather significant effort has been made to take advantage of the information related to the stages following hydraulic fracturing. Abbasi et al. (2014) developed a flowing material-balance model that is used to estimate fracture properties (i.e., half-length and storage coefficient) using early-time single-phase water flowback data. Ezulike et al. (2016) proposed a two-phase tank model for reducing the uncertainty in the estimated parameter and to calculate the stimulated fracture pore volume independently from fracture geometry. In all these recent research studies, several input data are generally unknown. Among them, fracture compressibility proved to be the least reliable. To bypass this problem, Fu et al. (2017) proposed a procedure to estimate the fracture compressibility by means of the so-called diagnostic fracturing injection test. More recently, pressure interference measurements between fractured horizontal wells have been used to estimate the geometrical characteristics of the induced hydraulic fractures (Kampfer and Dawson 2016; Roussel and Agrawal 2017; Seth et al. 2018). The after-closure pressure decline following hydraulic fracturing in "impulse fracture tests" (Nolte 1979) was also studied to determine formation permeability and fracture properties (Gu et al. 1993; Abousleiman et al. 1994). The latest work on this subject has been performed by Liu et al. (2017). In the latter, the dual-porosity/dual-permeability theory of poroelasticity is used to generate new after-closure pressure and pressure-derivative curves that are used to identify the flow regimes and then estimate formation properties. Pertaining to wellbore breathing, to the authors' best knowledge, no model has been provided to directly estimate fracture properties. Besides, breathing was used to capture in-situ stresses from mud losses encountered while drilling, as shown by Edwards et al. (2002) and Zoback et al. (2003). On the basis of their work, the concept of "accidental geomechanics" was further implemented by Majidi et al. (2015) to better tackle the challenges of drilling through depleted sands.

Mathematical Description

The focus is to model the response of an inclined wellbore drilled in a fractured formation and subjected to a 3D in-situ state of stress, as depicted in **Fig. 2.** As previously mentioned, when breathing happens, no appreciable flow occurs through the pores. Moreover, the mud may as well generate an impermeable layer (or an interfacial mudcake) between the fracture walls and the porous block, thus enhancing further isolation of the two phases. Under these conditions, we end up with a dual-porosity/single-permeability system. Interaction between the pore space and the fracture network will be limited to a poromechanical response only (Baldino et al. 2018; Meng et al. 2019). The extension of Biot's (1941) theory of linear poroelasticity to dual-porosity systems has been proposed by several authors (Aifantis 1979; Wilson and Aifantis 1982; Valliappan and Khalili-Naghadeh 1990; Berryman and Wang 1995; Bai et al. 1999). Analytical solutions based on the continuum model of Aifantis (1979) are available for a number of practical problems, including that of a wellbore drilled in a fractured formation (Wilson and Aifantis 1982; Li 2003; Abousleiman and Nguyen 2005; Nguyen et al. 2009; Liu and Abousleiman 2018). The proposed solution differs from those above in that it accounts for limited fluid discharge in the radial direction and single active permeability. Moreover, it bases its constitutive model on the Berryman and Wang (1995) stress formulation (as opposed to the strain formulation given by Aifantis 1979).

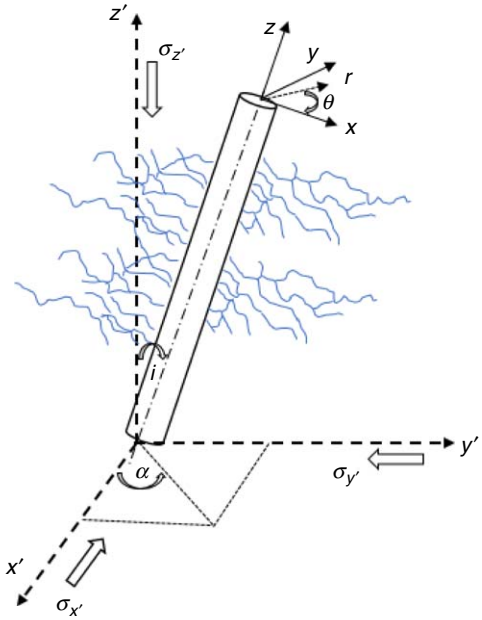

Fig. 2—Schematic of an inclined borehole drilled through an infinite medium with fracture networks of limited radial fluid discharge, and subjected to a nonhydrostatic state of stress.

Equilibrium Equations

To begin with, the equilibrium of forces is exactly the same as that derived for classical elasticity, in the absence of inertia and body forces (Sadd 2009),

$$\sigma_{ij,j} = \overline{0}. \quad \ldots\ldots (1)$$

The conservation of mass is described by the well-known continuity requirements for fluid phases, $m = 1, 2$.

$$\frac{\partial \zeta_m}{\partial t} + \frac{\partial q_i^{(m)}}{\partial x_i} = 0. \quad \ldots\ldots (2)$$

The subscript (or parenthetical superscript) "one" denotes the fractures, while "two" refers to the pores. The fluid increment of each phase is referred to as ζ_m, while $q_i^{(m)}$ is the fluid volume flux of each phase. In Eq. 2, no source terms accounting for interporosity communication are considered because the pores are assumed not to participate in fluid migration (Baldino et al. 2018). The conservation of linear momentum for the pore phase and fracture phase is given by the following equation:

$$q_i^{(m)} = -\frac{k_m}{\mu}\frac{\partial p_m}{\partial x_i}, \quad \ldots\ldots (3)$$

where k_m (in m^2) represents the permeability of each phase, μ (in Pa·s) is the dynamic viscosity of the mud, and p_m (in Pa) is the pore pressure. To express the fracture permeability in the case of a naturally fractured formation, the generalization of Muskat (1949), given by Jones (1975), can be used:

$$k_1 = \frac{h^3}{12\delta}, \quad \ldots\ldots (4)$$

where δ (in m) is the fracture spacing and h (in m) is the fracture aperture [which, in general, is a function of space and time, because it varies with the pressure distribution in the fractures, as shown by Baldino et al. (2018)]. It follows that the fracture porosity is given by

$$\phi_1 = \frac{h}{\delta}. \quad \ldots\ldots (5)$$

Constitutive Equations

The constitutive equations governing the response of the fractured medium can be expressed as follows (Aifantis 1979):

$$\sigma_{ij} = 2G\varepsilon_{ij} + 2G\frac{\nu}{1-2\nu}\varepsilon_{kk}\delta_{ij} - \sum_{m=1}^{2}\overline{\alpha}_m p_m \delta_{ij}. \quad \ldots\ldots (6)$$

The material properties G (in Pa) and ν are the shear modulus and Poisson's ratio, respectively, while $\overline{\alpha}_m$ is referred to as the generalized Biot-Willis coefficient for each phase. As mentioned, the constitutive model of Berryman and Wang (1995) is used to formulate the coupling between the state of deformation and the fluid flow in the two phases. Because of the choice of independent variables, the following is referred to as the stress formulation:

$$\zeta_1 = \overline{\alpha}_1 \varepsilon_{kk} + \frac{\overline{\alpha}_1}{B_{u1} K_{u1}} p_1$$
$$\zeta_2 = \overline{\alpha}_2 \varepsilon_{kk} + \frac{\overline{\alpha}_2}{B_{u2} K_{u2}} p_2. \quad \ldots\ldots (7)$$

In Eq. 7, ε_{kk} is the volumetric strain, K (in Pa) is the overall bulk modulus, and B_{u1} and B_{u2} are the generalized Skempton coefficients for the case of drained fractures/undrained matrix and drained matrix/undrained fractures, respectively. Similarly, K_{u1} (in Pa) and K_{u2} (in Pa) are the generalized undrained bulk moduli. The above coefficients can be expressed as a function of the volume fractions, and a few individual properties, as given in Appendix A.

Field Equations

Ultimately, it is worth noting that the strain/displacement relationship, as derived for classical elasticity, still holds (Sadd 2009).

$$\varepsilon_{ij} = \frac{1}{2}(u_{i,j} - u_{j,i}). \quad \ldots\ldots (8)$$

If the following assumptions are applied, the applicable field equations can be derived:

- Homogeneous and isotropic medium
- Laminar flow of Newtonian fluid in the fractures
- Dual porosity/single acting permeability (Baldino et al. 2018)
- Constant average fracture aperture
- No fracture propagation

$$G\nabla^2 u_i + (\lambda + G)\frac{\partial^2 u_j}{\partial x_i \partial x_j} = \overline{\alpha}_1 \frac{\partial p_1}{\partial x_i} + \overline{\alpha}_2 \frac{\partial p_2}{\partial x_i}$$
$$\frac{k_1}{\mu}\nabla^2 p_1 = \frac{\overline{\alpha}_1}{B_{u1} K_{u1}}\frac{\partial p_1}{\partial t} + \overline{\alpha}_1 \frac{\partial \varepsilon_{kk}}{\partial t}$$
$$\frac{\overline{\alpha}_2}{B_{u2} K_{u2}}\frac{\partial p_2}{\partial t} + \overline{\alpha}_2 \frac{\partial \varepsilon_{kk}}{\partial t} = 0. \quad \ldots\ldots (9)$$

Under the special circumstances (assumptions) given above, the solution technique follows that proposed by Cui et al. (1997), and then used by Abousleiman and Nguyen (2005) for dual-porosity media. Using a loading decomposition scheme, the problem is separated into three fundamental problems: (i) poroelastic plane strain, (ii) elastic uniaxial shear, and (iii) elastic antiplane shear. Because the focus falls on the pore-pressure distribution, we omit the solutions of the last two problems. The poroelastic plane-strain response is solved by superimposing the solution of three loading modes: (1) far-field isotropic stress, (2) virgin pore pressure, and (3) far-field stress deviator (Carter and Booker 1982; Detournay and Cheng 1988). An outline of the solution of each loading mode is given in Appendix B.

Final Pore-Pressure Solution

The final solution for the pore-pressure distribution in the fractures follows the superposition of the single solutions of the three modes:

$$p_1 = p_1^{(I)} = p_1^{(1)} + p_1^{(2)} + p_1^{(3)}. \quad \ldots\ldots (10)$$

This being said, it is worth further investigating the significance of $p_1^{(3)}$ (as given in Eq. B-11) when modeling borehole-breathing flowback scenarios. For this purpose, the set of data given in **Table 1** is used to determine $p_1^{(3)}$. In the work of Abousleiman and Nguyen (2005), an extremely small value of fracture permeability has been used (0.01 md). In this analysis, a small but more reasonable value (in terms of breathing phenomena) of 1 md is chosen to obtain the results shown in **Fig. 3.** As expected, the rate of dissipation of the induced pressure upon drilling increases with increasing fracture permeability [when compared to the results in the study by Abousleiman and Nguyen (2005)]. It can be observed how Mode 3 mostly influences the instantaneous drilling condition (very early time), in accordance with what has been observed by other authors (Detournay and Cheng 1988; Zhang et al. 2003; Abousleiman and Nguyen 2005). In contrast, the focus of this work falls on the flowback period for a borehole that has already been drilled. Moreover, when wellbore breathing is involved, it is expected to have much larger values of average fracture permeability, given the very short time frame of this event. Thus, it is reasonable to assume the pore pressure induced by Mode 3 to be completely dissipated by the time of flowback. For all these reasons, Eq. 10 can be approximated by

$$p_1 \approx p_1^{(2)}. \quad \ldots\ldots (11)$$

Flowback Type Curves

On the basis of the solution given in Eqs. B-7 and 11, the expression for the volumetric flow rate and the cumulative volume exchanged between fractures and wellbore is readily obtained (Baldino et al. 2018):

$$Q(t) = \frac{2\pi k_1}{\mu} H \left(r \frac{\partial p_1}{\partial r} \right)\Big|_{r_w} = \frac{4\pi k_1 H}{\mu}(p_1^0 - p_w) \sum_{n=1}^{\xi_n} \frac{J_1^2(\xi_n r_D)}{J_0^2(\xi_n r_w) - J_1^2(\xi_n r_D)} e^{-C_{11}^* \xi_n^2 t}. \quad \ldots\ldots (12)$$

$$\Delta V = \int_0^t Q(t)\mathrm{d}t = \frac{4\pi k_1 H}{\mu C_{11}^*}(p_1^0 - p_w) \cdot \left\{ \sum_{n=1}^{\xi_n} \frac{J_1^2(\xi_n r_D)}{[J_0^2(\xi_n r_w) - J_1^2(\xi_n r_D)]\xi_n^2} - \sum_{n=1}^{\xi_n} \frac{J_1^2(\xi_n r_D) e^{-C_{11}^* \xi_n^2 t}}{[J_0^2(\xi_n r_w) - J_1^2(\xi_n r_D)]\xi_n^2} \right\}. \quad \ldots\ldots (13)$$

Parameters	Values	Units
Matrix bulk modulus (K_2)	1100.0	MPa
Fractures bulk modulus (K_1)	550.0	MPa
Poisson's ratio (ν)	0.219	—
Matrix Biot's coefficient (α_2)	0.968	—
Matrix Skempton coefficient (B_2)	0.876	—
Fluid modulus (K_f)	1744.0	MPa
Fluid viscosity (μ)	0.001	Pa·s
Matrix porosity (ϕ_2)	0.14	Fraction
Fracture volume fraction (v_1)	0.014	Fraction
Fracture permeability (k_1)	9.87×10^{-16}	m^2
Initial pore pressure (p_0)	10.0	MPa
Vertical in-situ stress (σ_v)	29.0	MPa
Maximum horizontal stress (σ_H)	25.0	MPa
Minimum horizontal stress (σ_h)	20.0	MPa
Wellbore pressure (p_w)	0.0	MPa
Well azimuth (a)	30.0	degrees
Well Inclination (i)	60.0	degrees

Table 1—Input data, after Abousleiman and Nguyen (2005).

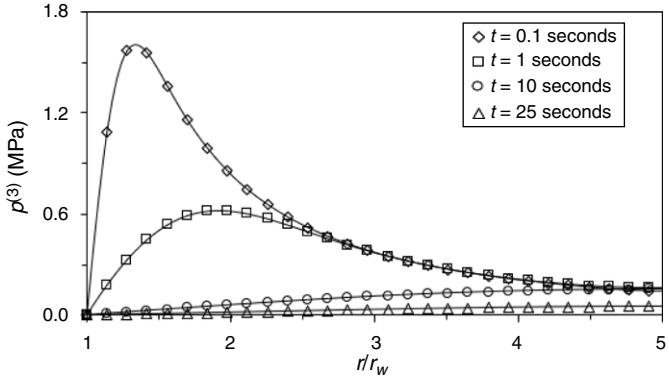

Fig. 3—Isochrones of the pore-pressure variation in the fractures, at $\theta = 0°$, for Mode 3, for $r_D = 5r_w$.

In Eqs. 12 and 13, H (in m) is the length of the openhole section. It shall be noted that the Hankel variable ξ_n has units of 1/m. The coefficient 4 multiplying Eq. 12 and Eq. 13 is a direct consequence of the application of the Bessel-function properties (Watson 1922), and it follows from the alternative formulation of $U'(\xi_n r_w)$ in Eq. 12 (Appendix B and Baldino et al. 2018). The generalized hydraulic diffusivity can be expressed as follows:

$$C_{11}^{*} = \frac{k_1}{\mu}\left(\frac{K_v M_1 + M_1 M_2 \overline{\alpha}_2^2}{\overline{\alpha}_1^2 M_1 + K_v + \overline{\alpha}_2^2 M_2}\right) = \frac{k_1}{\mu}\tilde{K}. \quad \ldots\ldots (14)$$

An introduction to the material coefficients in Eq. 14 is given in Appendix A. $K_v = 2G(1-\nu)/(1-2\nu)$ is the drained vertical bulk modulus (in Pa). With this in mind, Eqs. 12 and 13 can be manipulated to obtain the following dimensionless ($\tilde{Q}$) and dimensional [$\tilde{V}$ (in m^2), τ (in m^2)] groups:

$$\tilde{Q} = \frac{\mu Q(t)}{2\pi k_1 H(p_1^0 - p_w)} \quad \ldots\ldots (15a)$$

$$\tilde{V} = \frac{\Delta V}{2\pi H}\frac{C_{11}^{*}}{(p_1^0 - p_w)}\frac{\mu}{k_1} = \frac{\Delta V}{2\pi H}\frac{\tilde{K}}{(p_1^0 - p_w)} \quad \ldots\ldots (15b)$$

$$\tau = C_{11}^{*} t. \quad \ldots\ldots (15c)$$

where $\tilde{K}$, as defined in Eq. 14, has units of Pa and represents a generalized modulus of the nearby fractured formation. Its inverse can be referred to as a generalized total compressibility. Eqs. 15a and 15b can also be expressed as

$$\tilde{Q} = 2\sum_{n=1}^{\xi_n} \frac{J_1^2(\xi_n r_D)}{J_0^2(\xi_n r_w) - J_1^2(\xi_n r_D)} e^{-\xi_n^2 \tau} \quad (16a)$$

$$\tilde{V} = 2\left\{ \sum_{n=1}^{\xi_n} \frac{J_1^2(\xi_n r_D)}{[J_0^2(\xi_n r_w) - J_1^2(\xi_n r_D)]\xi_n^2} - \sum_{n=1}^{\xi_n} \frac{J_1^2(\xi_n r_D) e^{-\xi_n^2 \tau}}{[J_0^2(\xi_n r_w) - J_1^2(\xi_n r_D)]\xi_n^2} \right\}. \quad (16b)$$

Considering that monitoring of both pit volume gain and flow out is a primary method to detect fluid influxes (Cayeux and Daireaux 2013, 2016), along with the volume group given in Eq. 16b, the concept of pressure logarithmic derivatives is borrowed from well-test analysis (Tiab and Kumar 1980; Bourdet et al. 1989) to generate what will be referred to as volume-group derivatives.

$$\frac{\mathrm{d}(\tilde{V})}{\mathrm{d}\ln\tau} = \tau \frac{\mathrm{d}(\tilde{V})}{\mathrm{d}\tau} = \tau \tilde{Q}. \quad (17)$$

It should be noted that both $\tilde{V}$ and its derivative in Eq. 17 have the same units (m^2), and thus they can be plotted on the same graph, for different values of $\rho = r_D/r_w$. The volume group and its derivative are designed to represent the unique signature of borehole breathing during the flowback phase. To increase the accuracy of the unique signature match expected when breathing occurs and thus to also estimate the damaged radius, the dimensionless ratio $\tilde{V}/\tau\tilde{Q}$ is also plotted along with Eqs. 16b and 17. The latter concept has been borrowed from well-test analysis, and specifically from the pressure and pressure derivative ratio introduced by Onur and Reynolds (1988). For an 8½-in. (0.2159-m) borehole diameter, the flowback type curves in **Fig. 4** can be generated. From Fig. 4, it can be observed how the proposed wellbore-breathing model generates a unique signature, regardless of the drilling condition and formation properties. With type-curve matching of measured flowback data, a diagnostic procedure can thus be performed. If breathing is diagnosed, several in-situ properties can then be estimated by following the step-by-step procedure outlined below:

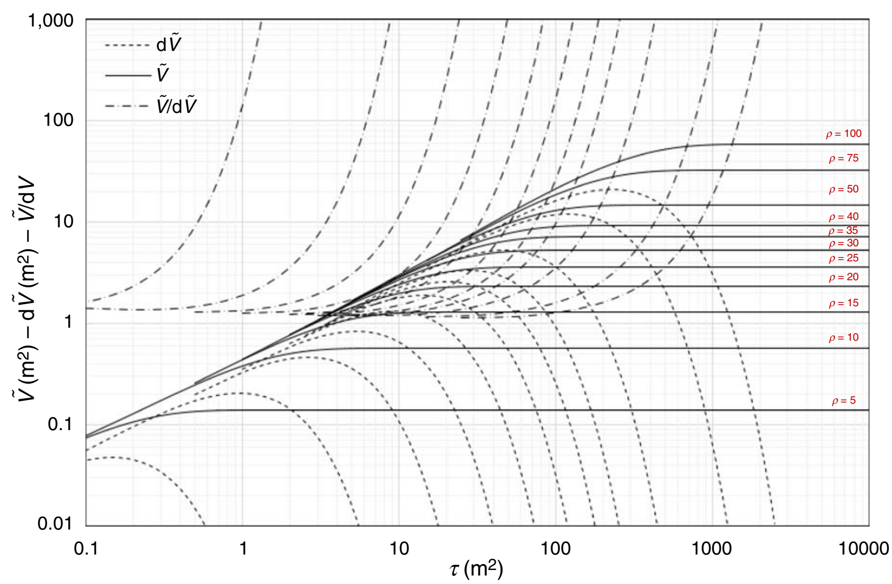

Fig. 4—Log-log diagnostic plot of flowback type curves for an 8½-in. borehole diameter. Volume group (continuous lines), volume-group derivative (dashed lines), and dimensionless ratio (dashed-dotted lines) are plotted for different $\rho = r_D/r_w$.

1. Collect the measured flowback signature (pit volume gain vs. time) and plot it on a log-log graph.
2. If returned flow-rate data are not measured along with the cumulative volume, perform numerical differentiation as shown in Appendix C and smoothing if necessary (generally flow data are quite noisy, and the noise is magnified when differentiation is performed). Plot the derivative data on the same log-log plot of the measured cumulative volume.
3. After checking that both type-curve plot and measured-data plot have the same number of decades (not necessarily the same decade values), proceed with curve matching by moving the measured-data plot along the x- and y-direction until a unique match is found and ρ is determined. If a unique match is achieved, then wellbore breathing is diagnosed.
4. Select any point in the graph and read the values of measured volume and $\tilde{V}$. Also, read the corresponding values of t and τ.
5. From volume match and Eq. 15b, evaluate the generalized total compressibility as follows:

$$\tilde{c} = \frac{1}{\tilde{K}} = \left[\frac{2\pi(p_1^0 - p_w)}{\Delta V} \tilde{V} \right]. \quad (18)$$

During flowback caused by borehole breathing, $p_1^0 > p_w$, and they are the hydrostatic pressure calculated from the ECD and ESD, respectively. It should be noted that for the induced fractures to completely close, the mud pressure must be lower than the stress acting normal to the fracture plane, also known as closure pressure (Hubbert and Willis 1957; Jaeger et al. 2009). In the breathing time frame, leakoff into the surrounding formation is often negligible. Hence, partially opened fractures are expected after the pumps are off and in the absence of drilling-fluid migration from the fractures into the rock matrix. The residual pore pressure in the fractures, just after flowback, is here assumed to be equal to the static wellbore pressure. The later diffusion of the excess pore pressure into the formation can be modeled following the approach of Liu et al. (2017). Only then will the induced fractures fully close. However, this goes beyond the life span of the loss/gain events treated in this work.

6. From time match and Eq. 15c, calculate the average borehole breathability (in m^3/s/Pa) (or a measure of the formation's tendency to allow drilling fluid to be transmitted, through the fractures, in and out of the borehole), using the total compressibility found in Step 5,

$$\beta_b = \frac{k_1}{\mu} H = \frac{\tau \tilde{c}}{t} H. \quad (19)$$

Because rheological properties of the drilling mud are generally known, a value of the apparent viscosity (Mitchell and Miska 2017) can be computed and used in Eq. 19 to estimate the average fracture permeability.

A more detailed flow chart is also provided in Appendix D.

Diagnostic Tool Application to Field Data

To have a better understanding of how the protocol works, the model is tested against four sets of field data published in the literature. In two of the four cases, the well was confirmed to suffer from borehole breathing. The remaining two cases are reported data of wells taking a gas kick. The first case study was reported by Ashley (2000), and it is related to the Jura-1 exploration well located offshore in the Northern Bonaparte Basin, Australia. Only the flowback signature is reported and no PWD data are available. The second case is regarding another offshore, deepwater well drilled in the Gulf of Mexico (GOM). PWD data were recorded, along with the pit volume gain (Ward and Clark 1998). The first of the kick data sets was published by Cayeux and Daireaux (2016), and it is regarding an offshore well drilled in the North Sea. Information has been reported before and after shut-in, including the pit volume gain. The second kick data set, and the last of the data sets, is related to an onshore well drilled in the Tarim Oil Field (China). The well was taking a gas kick, and the related data were published by Xingquan et al. (2015). Delta flow detection methods (Maus et al. 1979) were implemented, and thus only the recorded flow rates in and out of the well have been reported.

Case 1, Jura-1 Exploration Well. The exploration well was meant to provide an appraisal on the presence of hydrocarbons in the Flamingo and Plover Formations. The drilling site of Jura-1 was located in an area of good seismic-data quality, where potential fractured zones were supposed to be avoided.

After an intentional underbalanced period, from 2348-m depth, the well was drilled with an ECD equal to 1.25 s.g. (1250 kg/m^3 or 10.43 lbm/gal); s.g. stands for specific gravity. The static mud weight was equal to 1.15 s.g. (1150 kg/m^3 or 9.6 lbm/gal). In several occasions, downhole losses, followed by fluid regain, were recorded. In particular, the well was flow checked after reaching the 2520-m (8,265.6-ft) stand. The recorded flowback signature showed that approximately 12 bbl (or 1.82 m^3) of mud returned in 25 minutes. Because no flow-rate data were recorded, numerical differentiation is applied to obtain the Bourdet derivative of the measured cumulative volume. An interval length of 0.3 (see Appendix C) was chosen as the optimal length to smooth the volume-derivative data **(Fig. 5).** Both curves are plotted in the log-log diagnostic graph given in **Fig. 6.** The next step requires superimposing the log-log plot of the measured data to the type-curves plot shown in Fig. 4. The latter has been generated for an 8½-in. (0.2159-m) borehole, like the one of the Jura-1 well in the section experiencing breathing. **Fig. 7** shows that a unique match could be achieved between the field and type signatures. Wellbore breathing is hence diagnosed [and indeed breathing was confirmed to occur (Ashley 2000)]. This first case already suggests that wellbore breathing can be discerned by recognizing its unique signature. Using the proposed diagnostic tool, the operator needs only to enter the pit-volume-gain discrete data. Numerical derivatives of the volume and dimensionless ratio can then be computed automatically. The matching procedure can be performed manually or by digitizing the curve and seeking the minimum returned deviation. If a certain matching accuracy is set as a threshold, then breathing is diagnosed if matching is equal to or greater than its designated value. The existence of a unique match also gives us an estimate of the damaged radius $r_D = \rho r_w$. On the basis of Fig. 7, r_D equals 2.16 m (7.08 ft). By selecting A as the reference point for the best match that could be obtained by moving the measured data plot along the x- and y-direction, the values of the measured volume and $\tilde{V}$, and the corresponding values of t and τ, can be read as

$$\begin{cases} (\tilde{V})_A = 2.32 \text{ m}^2 \text{ and } (V)_A = 1.823 \text{ m}^3 \\ (\tau)_A = 18 \text{ m}^2 \text{ and } (t)_A = 1{,}655 \text{ seconds.} \end{cases} \quad (20)$$

On the basis of the given data (**Table 2**) and Eq. 18, an estimate of the in-situ total compressibility is found to be $\tilde{c} = 3.05 \times 10^{-10}$ Pa^{-1} (or 2.1×10^{-6} psi^{-1}). The average borehole breathability is estimated from the time match (Eq. 19), and it is $\beta = 5.70 \times 10^{-10}$ m^3/s/Pa (or 1.4825×10^{-3} bbl/min/psi). Finally, if the rheological properties of the drilling fluid are known, a value of the apparent viscosity (at the measured flow rate $Q_A = V'_A / t_A$) can be calculated. With the apparent viscosity, the permeability of the fractures can be estimated from Eq. 20. If the formation is expected to be naturally fractured, then the relations given in Eqs. 4 and 5 can be used to provide an estimate of the average fracture aperture and fracture spacing. On the basis of the estimated value of r_D, natural fractures seem likely (the formation was characterized by fractured zones). Moreover, after setting of the 9⅝-in. casing and drilling out of the shoe, a leak-off test (LOT) was performed, indicating a 1.6 s.g. (13.35 lbm/gal) fracture gradient. Considering that the 8½ in.; borehole suffering from breathing was drilled with an ECD up to 1.25 s.g. (10.43 lbm/gal), against a pore pressure between 1.13 and 1.27 s.g. (9.43–10.6 lbm/gal), natural fractures seem more likely to be the cause of the reported mud-loss/gain events. It should be noted that for naturally fractured formations, the fracture porosity is generally proportional to the matrix porosity. For instance, $\phi_1 = 0.1\phi_2$ for sedimentary rocks, and $\phi_1 = 10\phi_2$ for crystalline and metamorphic rocks (Elsworth and Bai 1992). Hence, if the matrix porosity is known, it would be possible to obtain an estimate of ϕ_1.

Case 2, GOM Offshore Well

The deepwater well was drilled with an 8½-in. section from 15,616 ft (4761 m) to 16,856 ft (or 5139 m) without experiencing unexpected flow returns. At that point, PWD was monitored during the connection, showing a 35-bbl (5.56-m^3) pit volume gain, because of the mud stored in the surface flowlines. Proceeding further, the PWD data showed an early indication of wellbore breathing. At the 16,877-ft (5253-m) stand, circulation was stopped and PWD clearly showed a significant breathing event. Approximately 85 bbl (13.5 m^3) of mud was returned, causing the ECD to decline exponentially to the ESD value, because of the extra frictional pressure losses introduced in the system. Once the 35 bbl of mud in the flowline is subtracted from the reported pit-volume-gain data, an approximated flowback signature can be found. In analogy to what had been done for Case 1, numerical differentiation is performed,

with an interval length of 0.3. Volume data vs. time and volume-derivative data vs. time are then plotted on a log-log graph (**Fig. 8**) and superimposed to the type curves, as shown in **Fig. 9.** From the unique match obtained, wellbore breathing is diagnosed (and indeed it was confirmed in the field operations). A damaged radius of 4.32 m (14.17 ft) is estimated from simple type-curve matching. By selecting B as the reference point, the values of the measured volume and $\tilde{V}$, and the corresponding values of t and τ, can be read.

$$\begin{cases} (\tilde{V})_B = 9.32 \text{ m}^2 \text{ and } (V)_B = 9.05 \text{ m}^3 \\ (\tau)_B = 118 \text{ m}^2 \text{ and } (t)_B = 1548.64 \text{ seconds.} \end{cases} \quad (21)$$

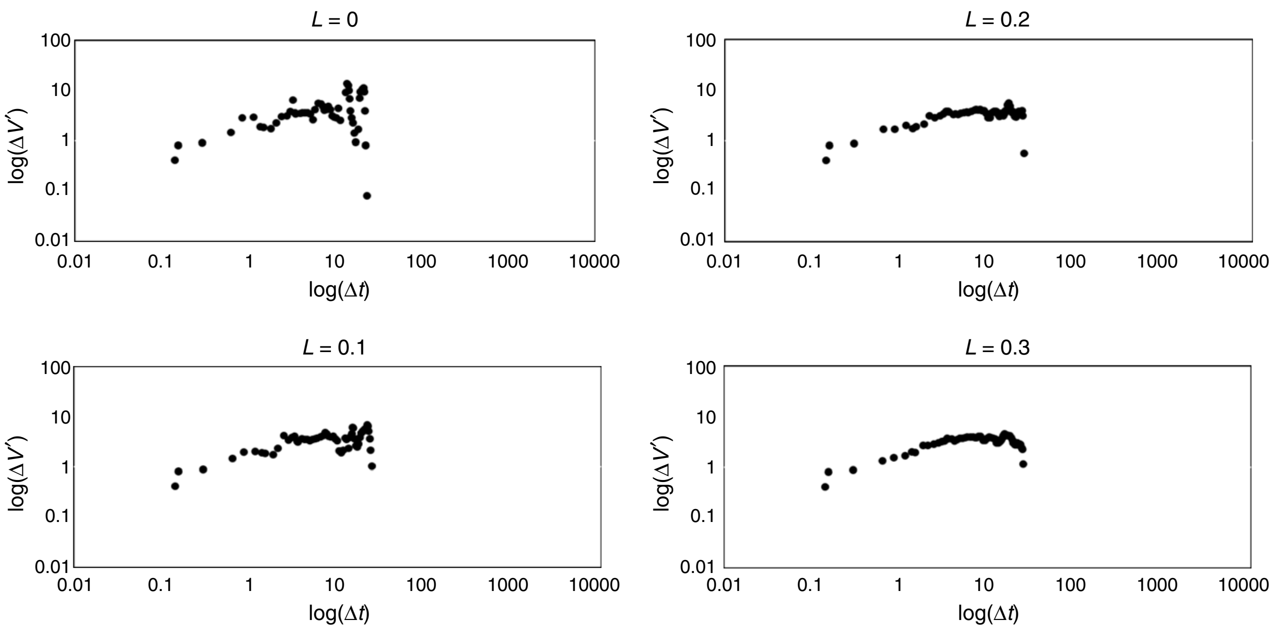

Fig. 5—Log-log plots of volume-derivative data for different interval lengths *L*.

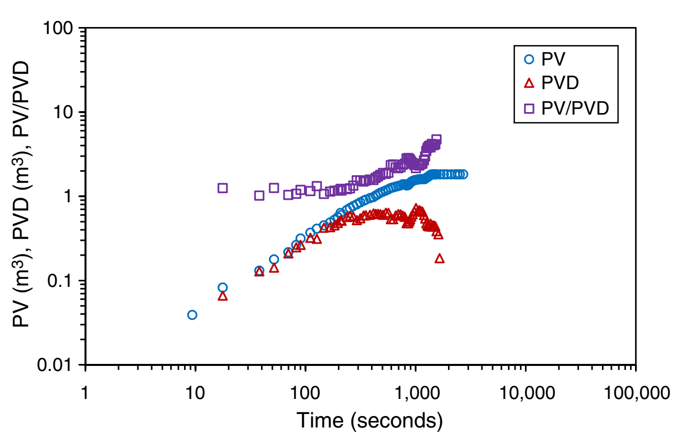

Fig. 6—Log-log plot of the measured volume and volume derivative for Jura-1 well.

On the basis of the given data (see **Table 3**) and Eq. 18, the total compressibility is found to be $\tilde{c} = 1.25 \times 10^{-10}$ Pa^{-1} (or 8.62×10^{-7} psi^{-1}). The latter value indicates a fairly stiff formation. This agrees with the relatively high fracturing pressure resulting from LOTs performed in the field. The LOTs carried out at 15,616 ft (4761 m) indicated a fracture pressure near 16.45 lbm/gal. The borehole-breathing events recorded while drilling this 8½-in. section showed that mud losses were experienced at approximately the same gradient. This indicates that fractures were most likely induced, and, by the estimated length of the damaged radius, they also might have propagated and intercepted already existing natural fractures (Brudy and Zoback 1999). The average borehole breathability resulting from time match is $\beta_b = 3.57 \times 10^{-9}$ m^3/s/Pa (or 9.30×10^{-3} bbl/min/psi). As expected, the borehole breathability is higher than the value estimated for the Jura-1 well. As β_b increases in magnitude, there is a higher tendency for loss/gain events to occur, and a larger amount of drilling fluid is exchanged. Unlike Case 1, PWD data are available here, and they can be used to further validate the ability of the proposed model to estimate representative in-situ formation properties. In fact, with the values obtained so far, it is possible to use Eqs. 12 and 14 to calculate the exponential decline of the ECD. With Eq. 12 and the assumption of a power-law fluid ($n = 0.6$ and $Ci = 0.5$ Pa·s^{-n}), we can calculate the pressure losses in the annulus generated by the returning mud (Mitchell and Miska 2017).

$$\frac{\mathrm{d}p_f}{\mathrm{d}s} = \left[\frac{4Q(t)}{\pi(d_c^2 - d_p^2)}\right]^n \frac{4Ci(8 + 4/n)^n}{(d_c - d_p)^{n+1}}, \quad (22)$$

where d_c and d_p are the casing and drillpipe diameters, respectively (for an 8½-in. borehole, it is common practice to have $d_p = 5$ in., while d_c is 9⅝ in.). The total wellbore pressure, including the extra contribution because of the additional frictional pressure losses, can be evaluated as

$$p_w = p_{w,ESD} + \Delta p_f(t). \quad (23)$$

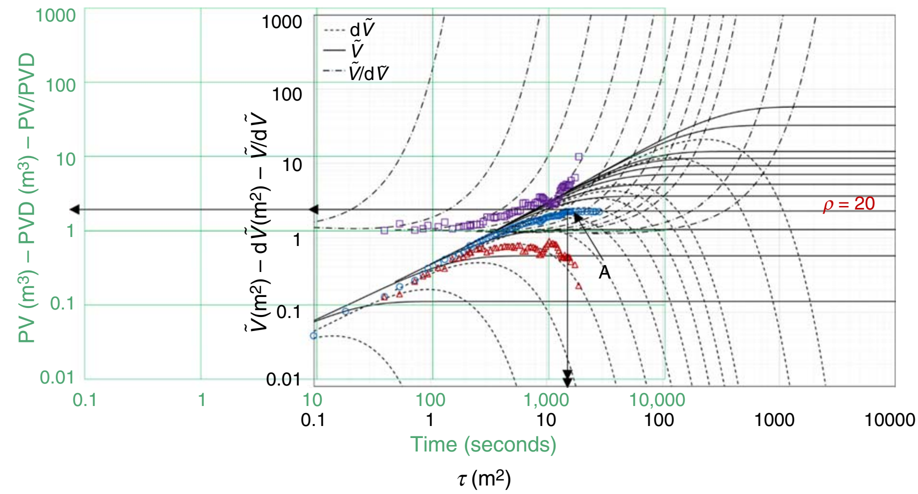

Fig. 7—Type-curve matching with measured data for Jura-1. The best match is obtained for $\rho = 20$.

Parameters	Values	Units
Openhole section (H)	172.0[a]	m
ECD	10.43[a]	lbm/gal
ESD	9.6[a]	lbm/gal
Volume group at point A ($\tilde{V}_A$)	2.32[b]	m^2
Measured pit volume at point A (V_A)	1.823[a,b]	m^3
Time group at point A (τ_A)	18.0[b]	m^2
Measured time at point A (V_A)	1655.0[a,b]	seconds

[a]Ashley (2000)
[b]From curves match

Table 2—Jura-1 exploration well input data.

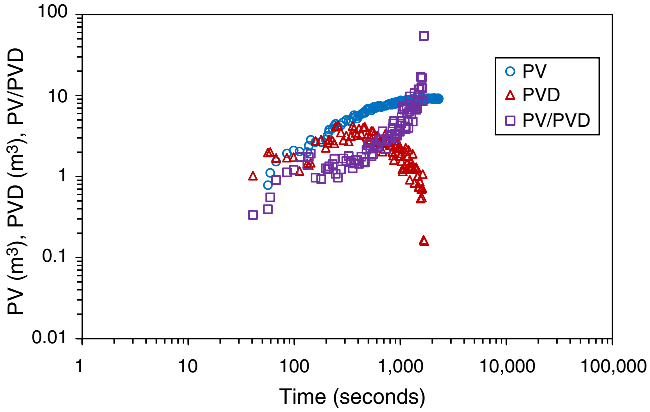

Fig. 8—Log-log plot of the measured volume and volume derivative for the GOM well.

Fig. 10 shows the comparison between measured and predicted ECD profile during the pumps-off time. Considering the inaccuracy of the inputs regarding the fluid rheological properties, the model is still able to give a promising prediction of the ECD decline. This shows that the parameter estimated in the previous steps is consistent and representative. Moreover, the exponential decline is quite well-mirrored.

Case 3, North Sea Offshore Well. This is the first case, treated here, of a well taking a kick during a connection (pumps shut down). At a measured depth (MD) of 2230 m, the open hole was 9½ in. (0.2413 m), and subsequently enlarged to 10⅝ in. (0.269875 m) by means of an under reamer. The gas reading was monitored during the last three stands, and the maximum value was recorded to be 2%.

Once the pumps were shut down to make a connection, a sudden increase in the pit volume was observed, and the connection procedure was aborted. Although circulation was re-established, the pit volume kept increasing, until the well became shut in. Fig. 11 shows the pit volume gain recorded during the aforementioned drilling operation. A quite marked monotonic increment of the pit volume can be observed. This is a first deviation from the typical signature that is recognizable for a general breathing event, where the pit volume gain flattens as the fractures get progressively depleted. However, once the wellbore was shut in, the pit volume gain eventually flattened to a constant value.

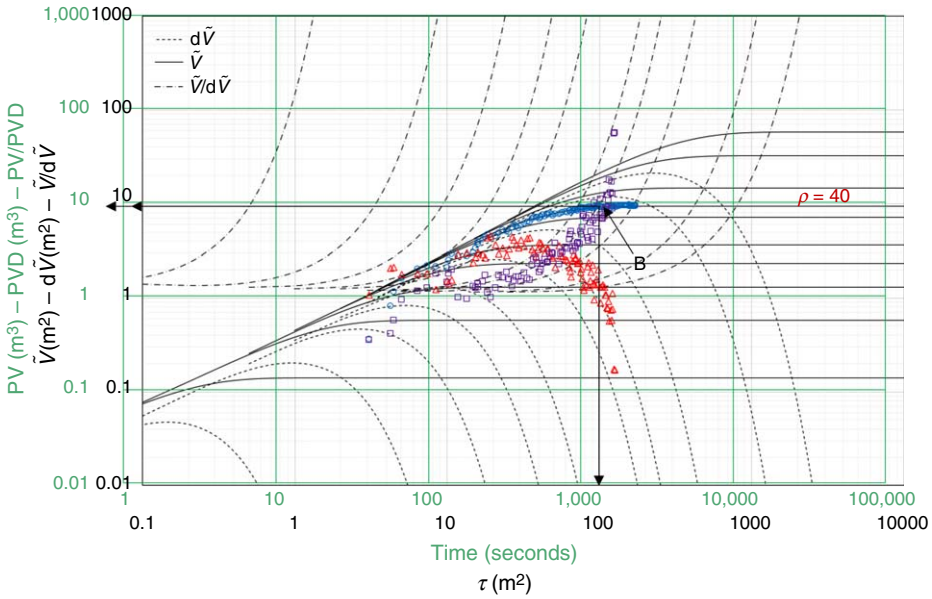

Fig. 9—Type-curve matching with measured data for the GOM well. The best match is obtained for $\rho = 40$.

Parameters	Values	Units
Openhole section (H)	492.0[a]	m
ECD	16.48[a]	lbm/gal
ESD	15.9[a]	lbm/gal
Openhole diameter ($2r_w$)	8.5[a]	in.
Casing inside diameter (d_c)	9.625[b]	in.
Drillpipe outside diameter (d_p)	5.0[b]	in.
Flow behavior index (n)	0.5[b]	—
Consistency index (C_i)	0.6[b]	$Pa \cdot s^{-n}$
Volume group at point A ($\tilde{V}_A$)	9.32[c]	m^2
Measured pit volume at point A (V_A)	9.05[a,c]	m^3
Time group at point A (τ_A)	118.0[c]	m^2
Measured time at point A (V_A)	1548.64[a,c]	seconds

[a]Ward and Clark (1998)
[b]Assumed
[c]From curves match

Table 3—Gulf of Mexico (GOM) offshore well input data.

In the absence of flow out data, the available volume data have been numerically differentiated and the diagnostic log-log plot in **Fig. 12** has been obtained. By a first look, a clear deviation from the typical breathing signature can be observed. Both the volume and volume derivative are increasing with increasing time, while during breathing the pit volume flattens and its derivative exponentially declines to zero. In addition, a clearly different trend of the dimensionless ratio can be appreciated. According to Fraser et al. (2014), approximately 70% of the reservoir influxes are experienced during connection times. This is caused by the loss of bottomhole pressure resulting from stopping the circulation (loss of hydraulic friction in the annulus). However, as shown in Case 2 (the deepwater GOM well), borehole breathing is also likely to occur at any pumps-off period, including connection time. If breathing is experienced, the effectiveness of kick fingerprinting could be jeopardized (Tarr et al. 2016). Hence, it could be beneficial to have a prompt answer from a breathing discriminator tool, able to quickly discern between the two influxes. The latter objective can be achieved by implementing the type-curve matching procedure formerly presented, as shown in **Fig. 13** (the type curves have been generated for a 10⅝-in. borehole).

From the signature's comparison, it can be observed that no unique match could be achieved. Despite a very similar trend displayed at the beginning of the influx, with increasing time, the deviation between the two signatures increases remarkably. The early-time similarities can be seen as the main cause behind the difficulties encountered in fingerprinting the nature of the influx. However, if the

dimensionless ratio is observed, the obvious decline occurring after the early stage clearly indicates a major signature difference. This means that flowing the well until the late time is not necessary to discern between breathing and a kick. Altogether, the type curves show how both the cumulative volume and its derivative deviate significantly from the expected behavior during breathing. The volume derivative registered a fast increment with time, while for a typical breathing case, it should decline exponentially to zero. Similarly, the cumulative volume recorded for this gas kick does not flatten with time (it flattens only after shut-in), whereas during breathing it is expected to have a stabilization of the pit volume to a constant value, after the differential pressure between fractures and borehole has been exhausted completely. Without a clear match of the signatures, the possibility of wellbore breathing then can be excluded.

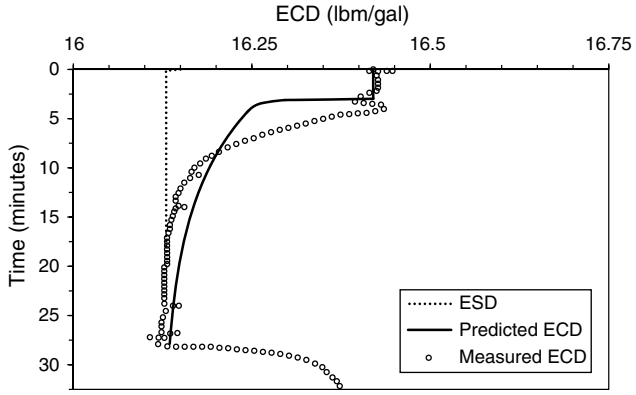

Fig. 10—PWD response comparison. The dashed line is the real PWD data (Ward and Clark 1998), the continuous line is the model output, and the dotted line is the square profile expected without breathing.

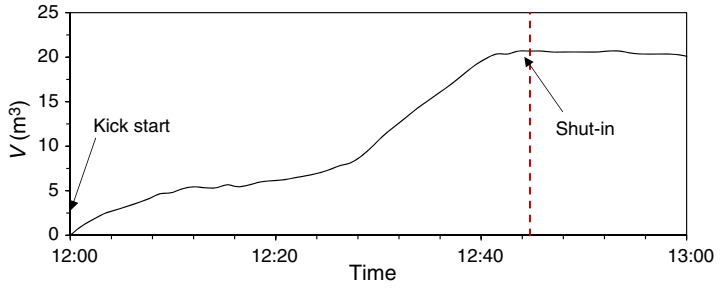

Fig. 11—Pit volume gain registered at the North Sea offshore well, after Cayeux and Daireaux (2016).

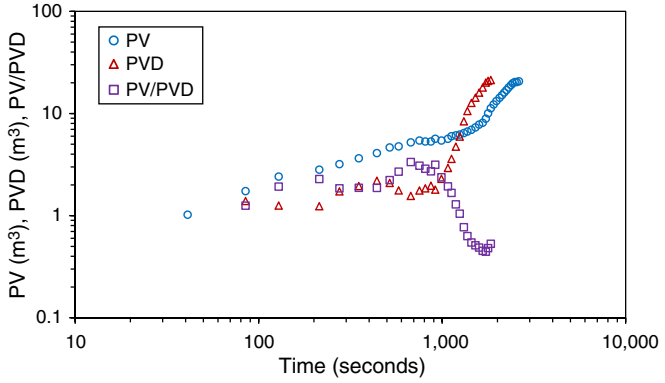

Fig. 12—Log-log plot of the measured volume and volume derivative for the North Sea well.

Case 4, Tarim Oil Field Onshore Well. The well is located in the Tarim Oil Field. The wellbore was drilled down to an MD of 5355 m and the kick-off point was set at 3890 m. The trajectory sequence was planned as follows: vertical, building up, steady inclined, horizontal section. The designed horizontal section is 998 m, and the maximum inclination angle is 87.99°. The production section was drilled using a drill bit with size of 6⅝ in. (0.168275 m). From the depth of 4307 m, managed-pressure technology was used to drill deeper. While drilling ahead, the out flow started to increase, and the recorded data are plotted in **Fig. 14.** Similarly to what was noticed in Case 3, both volume and volume derivative are increasing with increasing time, with no tendencies to invert the monotonic trend. In addition, a clearly different behavior of the dimensionless ratio can be seen, with a sudden decrease toward the late time.

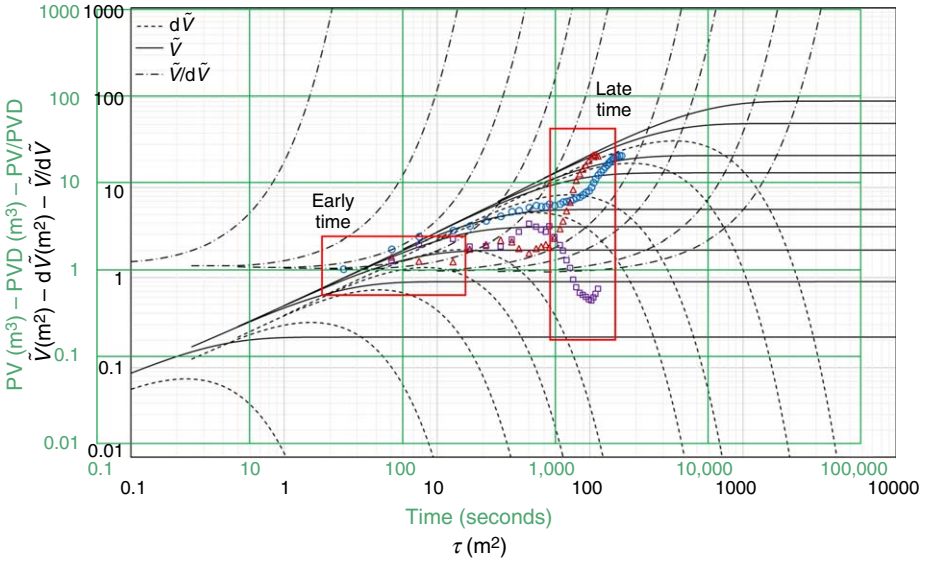

Fig. 13—Type-curve matching with measured data for the North Sea well. No match can be achieved between the two signatures.

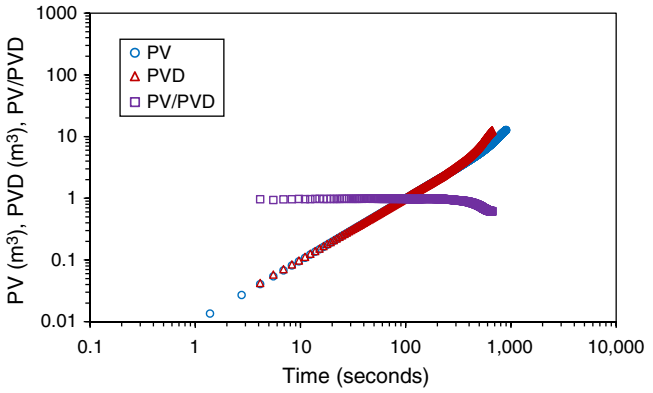

Fig. 14—Plot of measured flow out for the Tarim Oil Field well.

In analogy to what had been done for all previous cases, the log-log plot in Fig. 14 is superimposed on the type curves. The latter have been generated for a 6⅝-in. borehole. As expected, both the flow out and cumulative volume related to this gas-kick event show an evident difference in signature, if compared to the typical behaviors resulting from wellbore breathing **(Fig. 15).** It shall be again noted that at early times the signatures of a kick and of breathing look very similar in terms of the volume and volume derivative (see Figs. 13 and 15). This explains the difficulties generally encountered in discerning between a kick and a breathing event, particularly for exploration wells. Nonetheless, for this particular case, thanks to the dimensionless ratio, no unique match could be achieved even at early times; thus, the possibility of wellbore breathing can be excluded.

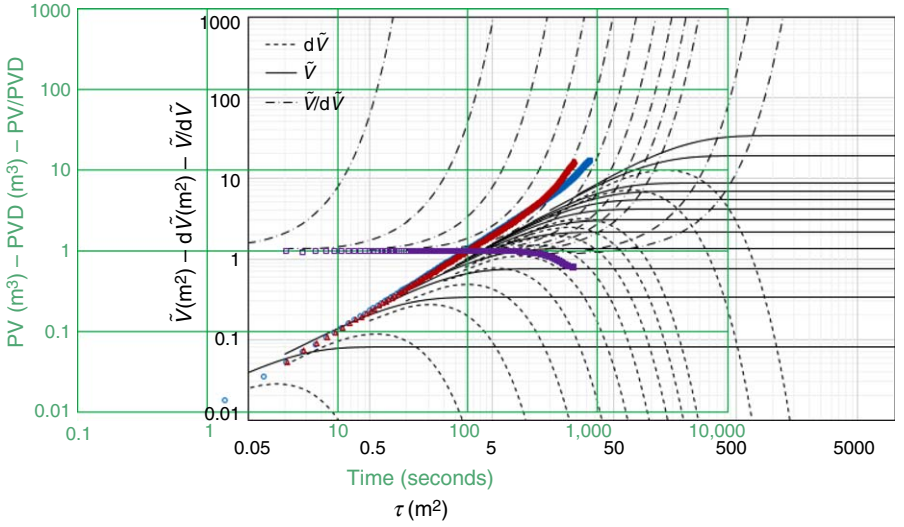

Fig. 15—Type-curve matching with measured data for the Tarim well. No match can be achieved between the flow-out signatures.

Conclusions

Whether one endorses a breathing model, such as the one presented in this work; other models in the literature, such as single-fracture models (Lavrov and Tronvoll 2005; Majidi et al. 2008; Ozdemirtas et al. 2009); or some synthesis of these, it is necessary to inquire into the benefits that a field engineer derives from its application. In this work, the proposed geomechanical model for borehole breathing has been effectively used as a diagnostic and formation-testing tool. On the basis of the model, flowback type curves have been generated for the purpose of applying a curve-matching technique with measured data. A step-by-step procedure has been outlined on how to use the provided type curves. For the ease of the matching operation (to help in getting a unique match, if any), it is recommended to plot the dimensionless ratio of the volume and volume derivative for both type curves and measured data. The advantage of the output is twofold: prompt discrimination between breathing and reservoir influx, and estimation of the damaged radius, generalized total compressibility, and average borehole breathability. The latter has been introduced as a measure of the formation's tendency to allow drilling fluid to be transmitted, through the fractures, in and out of the borehole. The proposed protocol has been tested on four sets of field data. When breathing cases were studied, the type curves proved to be very efficient in reproducing the unique signatures of both the volume and volume derivative. For the second breathing data set, the estimated formation properties have been used to predict the ECD exponential decline. The latter was then compared to the actual measured ECD profile, showing quite promising results despite the absence of information related to the drilling-fluid rheological properties. When kick cases were analyzed, the flowback type curves showed a distinct deviation, especially at late times, between the volume and volume-derivative behaviors characterizing a kick; thus, a direct and rapid discrimination between the two influxes can be obtained. Moreover, basing the diagnosis on trend matching makes this protocol easy to automate, and therefore makes it potentially applicable for real-time monitoring.

Nomenclature

B_{um} = generalized Skempton coefficient of phase m
$\tilde{c}$ = generalized total compressibility, Pa^{-1}
Ci = consistency index, $Pa{\cdot}s^{-n}$
C_{11}^{*} = generalized consolidation coefficient, m^2/s
D_0 = deviatoric stress, Pa
G = shear modulus, Pa
h = fracture aperture, m
H = openhole section length, m
$H[f]$ = Hankel transform
H_0 = mean hydrostatic stress, Pa
i = wellbore inclination angle, degrees
J_ν = Bessel function of first kind, of order ν
k_m = phase permeability, m^2
K = bulk modulus, Pa
$\tilde{K}$ = generalized total bulk modulus, Pa
K_f = fluid modulus, Pa
K_{um} = generalized undrained bulk modulus of phase m, Pa
n = behavior index
p_m = phase pore pressure, Pa
p_{m0} = initial phase pore pressure, Pa
p_w = wellbore pressure, Pa
P_D = dimensional pressure group, Pa
$q_i^{(m)}$ = volumetric flux of phase m in i-direction, ft/min
Q = volumetric flow rate, m^3/s
$\tilde{Q}$ = dimensionless flow rate
r_w = wellbore radius, m
r_D = damaged radius, m
s = Laplace variable, s^{-1}
S_{ij} = local stress tensor components, Pa
u_i = solid displacement, m
V = cumulative volume, m^3
$\tilde{V}$ = dimensional volume group, m^2
v_m = phase volume fraction
Y_ν = Bessel function of second kind, of order ν
α = wellbore azimuth angle, degrees
α_m = classical Biot-Willis coefficient of phase m
β = drilling-fluid compressibility, Pa^{-1}
$\overline{\alpha}_m$ = generalized Biot-Willis coefficient of phase m
β_b = borehole breathability, $m^3/s/Pa$
γ = fracture compressibility, Pa^{-1}
δ = fracture spacing, m
δ_{ij} = Kronecker delta
ε_{ij} = strain-tensor components
ε_{kk} = normal strain summation
ζ_m = increment of fluid content of phase m
θ = angle around borehole, degrees
θ_r = angle of rotation between the wellbore axes and the in-situ-stress directions, degrees
σ_{ij} = stress-tensor components, Pa
σ_{kk} = normal stresses summation, Pa
λ = Lamé coefficient, Pa
μ = fluid dynamic viscosity, Pa·s

ν = Poisson's ratio
ξ_n = Hankel's variable, m^{-1}
τ = dimensional time group, m^2
ϕ_m = phase porosity

Acknowledgments

The authors are thankful to the Tulsa University Drilling Research Projects (TUDRP) member companies for their technical and financial support. They also thank Meng Meng and Xingquan Zhang for the very helpful discussion regarding the field data of Case 4.

References

Aadnøy, B. S. 2010. Appendix B: Evaluation of Ballooning in Deep Wells. In *Modern Well Design*, second edition, 285–294. New York City: CRS Press.

Abbasi, M. A., Ezulike, D. N., Dehghanpour, H. et al. 2014. A Comparative Study of Flowback Rate and Pressure Transient Behavior in Multifractured Horizontal Wells Completed in Tight Gas and Oil Reservoirs. *J Nat Gas Sci Eng* **17:** 82–93. https://doi.org/10.1016/j.jngse.2013.12.007.

Abousleiman, Y., Cheng, A. D., and Gu, H. 1994. Formation Permeability Determination by Micro or Mini-Hydraulic Fracturing. *J Energy Resour Technol* **116** (2): 104–114. https://doi.org/10.1115/1.2906014.

Abousleiman, Y. and Nguyen, V. 2005. Poromechanics Response of Inclined Wellbore Geometry in Fractured Porous Media. *J Eng Mech* **131** (11): 1170–1183. https://doi.org/10.1061/(ASCE)0733-9399(2005)131:11(1170).

Aifantis, E. C. 1979. On the Response of Fissured Rocks. *Dev Mech* **10** (1): 249–253.

Ashley, P. R. 2000. Well Control of an Influx From a Fracture Breathing Formation. Presented at the IADC/SPE Asia Pacific Drilling Technology, Kuala Lumpur, Malaysia, 11–13 September. SPE-62770-MS. https://doi.org/10.2118/62770-MS.

Babu, D. R. 1998. Effect of P–ρ–T Behavior of Muds on Loss/Gain During High-Temperature Deep-Well Drilling. *J Pet Sci Eng* **20** (1-2): 49–62. https://doi.org/10.1016/S0920-4105(98)00003-5.

Bai, M., Abousleiman, Y., Cui, L. et al. 1999. Dual-Porosity Poroelastic Modeling of Generalized Plane Strain. *Int J Rock Mech Min Sci* **36** (8): 1087–1094. https://doi.org/10.1016/S1365-1609(99)00065-9.

Baldino, S. and Miska, S. Z. 2018. Dual Porosity/Single Permeability Poromechanics Response of an Inclined Wellbore With No-Flow Outer Boundary. In *Micro to MACRO Mathematical Modelling in Soil Mechanics*, eds. P. Giovine, P. M. Mariano, and G. Mortara, Chapter 4, 35–48. Cham, Switzerland: Birkhäuser.

Baldino, S., Miska, S. Z., and Ozbayoglu, E. 2018. A Novel Approach to Borehole Breathing Investigation in Naturally Fractured Formations. *SPE Drill & Compl* **34** (1): 27–45 SPE-189661-PA. https://doi.org/10.2118/189661-PA.

Berryman, J. G. and Wang, H. F. 1995. The Elastic Coefficients of Double-Porosity Models for Fluid Transport in Jointed Rock. *J Geophys Res* **100** (812): 24611–24627. https://doi.org/10.1029/95JB02161.

Biot, M. A. 1941. General Theory of Three-Dimensional Consolidation. *J Appl Phys* **12** (2): 155–164.

Bourdet, D., Ayoub, J. A., and Pirard, Y. M. 1989. Use of Pressure Derivative in Well Test Interpretation. *SPE Form Eval* **4** (2): 293–302. SPE-12777-PA. https://doi.org/10.2118/12777-PA.

Brudy, M. and Zoback, M. 1999. Drilling-Induced Tensile Wall-Fractures: Implications for Determination of In-Situ Stress Orientation and Magnitude. *Int J Rock Mech Min Sci* **36** (2): 191–215. https://doi.org/10.1016/S0148-9062(98)00182-X.

Carter, J. P. and Booker, J. R. 1982. Elastic Consolidation Around a Deep Circular Tunnel. *Int J Solids Struct* **18** (12): 1059–1074. https://doi.org/10.1016/0020-7683(82)90093-2.

Cayeux, E. and Daireaux, B., 2013. Precise Gain and Loss Detection Using a Transient Hydraulic Model of the Return Flow to the Pit. Presented at the SPE/IADC Middle East Drilling Technology Conference & Exhibition, Dubai, UAE, 7–9 October. https://doi.org/10.2118/166801-MS.

Cayeux, E. and Daireaux, B. 2016. Insights Into the Physical Phenomena That Influence Automatic Gain/Loss Detection During Drilling Operations. *SPE Drill & Compl* **32** (1): 13–24. SPE-166801-PA. https://doi.org/10.2118/166801-PA.

Cui, L., Cheng, A. H., and Abousleiman, Y. 1997. Poroelastic Solution for an Inclined Borehole. *J Appl Mech* **64** (1): 32–38. https://doi.org/10.1115/1.2787291.

Dalton, C. L., Paulk, M. D., and Bittar, M. 2002. Real-Time, Time-Lapse Resistivity Logging With a Wired Composite Tubing. Presented at the SPE International Petroleum Conference and Exhibition in Mexico, Villahermosa, Mexico, 10–12 February. https://doi.org/10.2118/74380-MS.

Detournay, E. and Cheng, A. D. 1988. Poroelastic Response of a Borehole in a Non-Hydrostatic Stress Field. *Int J Rock Mech Min Sci Geomech Abstr* **25** (3): 171–182. https://doi.org/10.1016/0148-9062(88)92299-1.

Edwards, S. T., Bratton, T. R., and Standifird, W. B. 2002. Accidental Geomechanics-Capturing In-Situ Stress From Mud Losses Encountered While Drilling. Presented at the SPE/ISRM Rock Mechanics Conference, Irving, Texas, 20–23 October. SPE-78205-MS. https://doi.org/10.2118/78205-MS.

Elsworth, D. and Bai, M. 1992. Flow-Deformation Response of Dual-Porosity Media. *J Geotech* **118** (1): 107–124. https://doi.org/10.1061/(ASCE)0733-9410(1992)118:1(107).

Erivwo, O. E. and Adeleye, O. A. 2012. Narrow Margin Drilling in Deepwater: Solution Concepts. Presented at the SPE Deepwater Drilling and Completions Conference, Galveston, Texas, 2USA, 20–21 June. SPE-156254-MS. https://doi.org/10.2118/156254-MS.

Ezulike, O., Dehghanpour, H., Virues, C. et al. 2016. Flowback Fracture Closure: A Key Factor for Estimating Effective Pore Volume. *SPE Res Eval & Eng* **19** (4): 567–582. SPE-175143-PA. https://doi.org/10.2118/175143-PA.

Fraser, D., Lindley, R., Moore, D. et al. 2014. Early Kick Detection Methods and Technologies. Presented at the SPE Annual Technical Conference and Exhibition, Amsterdam, The Netherlands, 27–29 October. SPE-170756-MS. https://doi.org/10.2118/170756-MS.

Fu, Y., Dehghanpour, H., Ezulike, D. O. et al. 2017. Estimating Effective Fracture Pore Volume From Flowback Data and Evaluating its Relationship to Design Parameters of Multistage-Fracture Completion. *SPE Prod & Oper* **32** (4): 423–439. SPE-175892-PA. https://doi.org/10.2118/175892-PA.

Gale, J. F., Laubach, S. E., Olson, J. E. et al. 2014. Natural Fractures in Shale: A Review and New Observations. *Am Assoc Pet Geol Bull* **98** (11): 2165–2216. https://doi.org/10.1306/08121413151.

Gill, J. A. 1989. How Borehole Ballooning Alters Drilling Responses. *Oil Gas J* **87** (11): 43–52.

Golwalkar, A., Lang, C. M., Doodraj, S. et al. 2016. Exploratory Drilling in Severely Ballooning Formation—Use of Best Drilling Practices and Real Time Monitoring for Low Cost Mitigation. Presented at the International Petroleum Technology Conference, Bangkok, Thailand, 14–16 November. IPTC-18763-MS. https://doi.org/10.2523/IPTC-18763-MS.

Gu, H., Elbel, J. L., Nolte, K. G. et al. 1993. Formation Permeability Determination Using Impulse-Fracture Injection. Presented at the SPE Production Operations Symposium, Oklahoma City, Oklahoma, 21–23 March. SPE-25425-MS. https://doi.org/10.2118/25425-MS.

Helstrup, O. A., Rahman, M. K., Hossain, M. M. et al. 2001. A Practical Method for Evaluating Effects of Fracture Charging and/or Ballooning When Drilling High Pressure, High Temperature (HPHT) Wells. Presented at the SPE/IADC Drilling Conference, Amsterdam, Netherlands, 27 February–1 March. SPE-67780-MS. https://doi.org/10.2118/67780-MS.

Huang, J., Griffiths, D. V., and Wong, S. W. 2011. Characterizing Natural-Fracture Permeability From Mud-Loss Data. *SPE J.* **16** (1): 111–114. SPE-139592-PA. https://doi.org/10.2118/139592-PA.

Hubbert, M. K. and Willis, D. G. 1957. Mechanics of Hydraulic Fracturing. In *Petroleum Transactions, AIME,* Vol. 210, 153–168, SPE-686-G. [Paper presented at the Petroleum Branch Fall Meeting, Los Angeles, California, 14–17 October.]

Jaeger, J. C., Cook, N. G., and Zimmerman, R. 2009. *Fundamentals of Rock Mechanics*. John Wiley & Sons.

Jamison, W. and Azad, A. 2017. The Hydraulic Fracture–Natural Fracture Network Configuration in Shale Reservoirs: Geological Limiting Factors. *J Pet Sci Eng* **159:** 205–229. https://doi.org/10.1016/j.petrol.2017.09.017.

Johnson, A., Leuchtenberg, C., Petrie, S. et al. 2014. Advancing Deepwater Kick Detection. Presented at the IADC/SPE Drilling Conference and Exhibition, Fort Worth, Texas, 4-6 March. SPE-167990-MS. https://doi.org/10.2118/167990-MS.

Jones Jr., F. O. 1975. A Laboratory Study of the Effects of Confining Pressure on Fracture Flow and Storage Capacity in Carbonate Rocks. *J Pet Technol* **27** (1): 21–27. SPE-4569-PA. https://doi.org/10.2118/4569-PA.

Kampfer, G. and Dawson, M. 2016. A Novel Approach to Mapping Hydraulic Fractures Using Poromechanic Principles. Presented at the 50th U.S. Rock Mechanics/Geomechanics Symposium, Houston, Texas, 26–29 June.

Karstad, E. 1998. Analysis of Ballooning Effects During Drilling of High Pressure High Temperature Wells. Presented at the European Petroleum Conference, The Hague, Netherlands, 20–22 October. SPE-52066-STU. https://doi.org/10.2118/52066-STU.

Lavrov, A. and Tronvoll, J. 2005. Mechanics of Borehole Ballooning in Naturally-Fractured Formations. Presented at the SPE Middle East Oil and Gas Show and Conference, Kingdom of Bahrain, 12–15 March. SPE-93747-MS. https://doi.org/10.2118/93747-MS.

Li, X. 2003. Consolidation Around a Borehole Embedded in Media With Double Porosity Under Release of Geostatic Stresses. *Mechanics Research Communications* **30** (1): 95–100. https://doi.org/10.1016/S0093-6413(02)00315-4.

Liétard, O., Unwin, T., Guillot, D. et al. 1996. Fracture Width LWD and Drilling Mud/LCM Selection Guidelines in Naturally Fractured Reservoirs. Presented at the European Petroleum Conference, Milan, Italy, 22–24 October. SPE-36832-MS. https://doi.org/10.2118/36832-MS.

Liétard, O., Unwin, T., Guillot, D. J. et al. 1999. Fracture Width Logging While Drilling and Drilling Mud/Loss-Circulation-Material Selection Guidelines in Naturally Fractured Reservoirs (includes associated papers 75283, 75284, 81590 and 81591). *SPE Drill & Compl* **14** (3): 168–177. SPE-57713-PA. https://doi.org/10.2118/57713-PA.

Liu, C., Mehrabian, A., and Abousleiman, Y. N. 2017. Poroelastic Dual-Porosity/Dual-Permeability After-Closure Pressure-Curves Analysis in Hydraulic Fracturing. *SPE J.* **22** (1): 198–218. SPE-181748-PA. https://doi.org/10.2118/181748-PA.

Liu, C. and Abousleiman, Y. N. 2018. Multiporosity/Multipermeability Inclined-Wellbore Solutions With Mudcake Effects. *SPE J.* **23** (5): 1723–1747. SPE-191135-PA. https://doi.org/10.2118/191135-PA.

Majidi, R., Miska, S. Z., Yu, M. et al. 2008. Fracture Ballooning in Naturally Fractured Formations: Mechanism and Controlling Factors. Presented at the SPE Annual Technical Conference and Exhibition, Denver, Colorado, 21–24 September. SPE-115526-MS. https://doi.org/10.2118/115526-MS.

Majidi, R., Miska, S., Thompson, L. G. et al. 2010. Quantitative Analysis of Mud Losses in Naturally Fractured Reservoirs: The Effect of Rheology. *SPE Drill & Compl* **25** (4): 509–517. SPE-114130-PA. https://doi.org/10.2118/114130-PA.

Majidi, R., Edwards, S., Zhang, J. et al. 2015. Drilling Depleted Sands: Geomechanics, Challenges and Mitigations. Presented at the SPE Annual Technical Conference and Exhibition, Houston, Texas, 28–30 September. SPE-174741-MS. https://doi.org/10.2118/174741-MS.

Maus, L. D., Tannich, J. D., and Ilfrey, W. T. 1979. Instrumentation Requirements for Kick Detection in Deep Water. *J Pet Technol* **31** (8): 1029–1034. SPE-7238-PA. https://doi.org/10.2118/7238-PA.

Meng, M., Baldino, S., Miska, S. Z. et al. 2019. Wellbore Stability in Naturally Fractured Formations Featuring Dual-Porosity/Single-Permeability and Finite Radial Fluid Discharge. *J Pet Sci Eng* **174:** 790–803. https://doi.org/10.1016/j.petrol.2018.11.088.

Mi, L., An, C., Cao, Y., et al. 2016. A Guideline on Optimizing Fracture Modeling for Fractured Reservoir Simulation. Presented at the SPE Asia Pacific Hydraulic Fracturing Conference, Beijing, China, 24–26 August. SPE-181814-MS. https://doi.org/10.2118/181814-MS.

Mitchell, R. F. and Miska, S. Z. 2017. *Fundamentals of Drilling Engineering*, No. 12. Richardson, Texas: SPE Textbook Series, Society of Petroleum Engineers.

Muskat, M. 1949. *Physical Principles of Oil Production*, New York: McGraw-Hill Book Co., Inc.

Nguyen, V. X., Abousleiman, Y. N., and Hoang, S. 2009. Analyses of Wellbore Instability in Drilling Through Chemically Active Fractured-Rock Formations. *SPE J.* **14** (2): 283–301. SPE-105383-PA. https://doi.org/10.2118/105383-PA.

Nolte, K. G. 1979. Determination of Fracture Parameters From Fracturing Pressure Decline. Presented at the SPE Annual Technical Conference and Exhibition, Las Vegas, Nevada, 23–26 September. SPE-8341-MS. https://doi.org/10.2118/8341-MS.

Onur, M. and Al-Saddique, M. 1999. Comparison of Derivative Algorithms Used in Pressure Transient Analysis. *Arab J Sci Eng* **24** (1 B): 59–78.

Onur, M. and Reynolds, A. C. 1988. A New Approach for Constructing Derivative Type Curves For Well Test Analysis. *SPE Form Eval* **3** (1): 197–206. SPE-16473-PA. https://doi.org/10.2118/16473-PA.

Ozdemirtas, M., Babadagli, T., and Kuru, E. 2009. Experiemental and Numerical Investigations of Borehole Ballooning in Rough Fractures. *SPE Drill & Compl* **24** (2): 256–265. SPE-110121-PA. https://doi.org/10.2118/110121-PA.

Power, D., Ivan, C. D., and Brooks, S. W. 2003. The Top 10 Lost Circulation Concerns in Deepwater Drilling. Presented at the SPE Latin American and Caribbean Petroleum Engineering Conference, Port-of-Spain, Trinidad and Tobago, 27–30 April. SPE-81133-MS. https://doi.org/10.2118/81133-MS.

Rice, J. R. and Cleary, M. P. 1976. Some Basic Stress Diffusion Solutions for Fluid-Saturated Elastic Porous Media With Compressible Constituents. *Rev Geophys* **14** (2): 227–241. https://doi.org/10.1029/RG014i002p00227.

Rosenberg, S. M. and Gala, D. M. M. 2011. Liner Drilling Technology as a Mitigation to Wellbore Ballooning—A Successful Case Study in the Gulf of Mexico Shelf. Presented at the SPE/IADC Drilling Conference and Exhibition, Amsterdam, The Netherlands, 1–3 March. SPE-140261-MS. https://doi.org/10.2118/140261-MS.

Roussel, N. P. and Agrawal, S. 2017. Introduction to Poroelastic Response Monitoring—Quantifying Hydraulic Fracture Geometry and SRV Permeability From Offset-Well Pressure Data. Presented at the SPE/AAPG/SEG Unconventional Resources Technology Conference, Austin, Texas, 24–26 July. URTEC-2645414-MS. https://doi.org/10.15530/URTEC-2017-2645414.

Sadd, M. H. 2009. *Elasticity: Theory, Applications, and Numerics*. Oxford: Academic Press.

Samuel, R. 2018. Early Kick Detection Using Adaptive Analytics With Downhole Accelerometer Data. Presented at the SPE Annual Technical Conference and Exhibition, Dallas, Texas, 24–26 September. SPE-191645-PA. https://doi.org/10.2118/191645-MS.

Segatto, M. and Colombo, I. 2011. Use of Reservoir Simulation to Help Gas Shale Reserves Estimation. Presented at the International Petroleum Technology Conference, Bangkok, Thailand, 15–17 November. IPTC-14789-MS. https://doi.org/10.2523/IPTC-14798-MS.

Seth, P., Manchanda, R., Kumar, A. et al. 2018. Estimating Hydraulic Fracture Geometry by Analyzing the Pressure Interference Between Fractured Horizontal Wells. Presented at the SPE Annual Technical Conference and Exhibition, Dallas, Texas, 24–26 September. SPE-191492-MS. https://doi.org/10.2118/191492-MS.

Stehfest, H. 1970. Algorithm 368: Numerical Inversion of Laplace Transforms [D5]. *Commun ACM* **13** (1), 47–49.

Tare, U. A., Whitfill, D. L., and Mody, F. K. 2001, Drilling Fluid Losses and Gains: Case Histories and Practical Solutions. Presented at the SPE Annual Technical Conference and Exhibition, New Orleans, Louisiana, 30 September–3 October. SPE-71368-MS. https://doi.org/10.2118/71368-MS.
Tarr, B. A., Ladendorf, D. W., Sanchez, D. et al. 2016. Next-Generation Kick Detection During Connections: Influx Detection at Pumps Stop (IDAPS) Software. *SPE Drill & Compl* **31** (4): 250–260. SPE-178821-PA. https://doi.org/10.2118/178821-PA.
Tiab, D. and Kumar, A. 1980. Application of the p'_D Function to Interference Analysis. *J Pet Technol* **32** (8): 1465–1470. SPE-6053-PA. https://doi.org/10.2118/6053-PA.
Tirado Vargas, G. R., Lupo, C. P. M., Beltran, J. C. et al. 2011. MPD Makes Possible to Drill and Trip Out of the Hole in a Gas Well With a Combination of a Narrow Mud Weight Window and a Serious Ballooning Effect. Presented at the IADC/SPE Managed Pressure Drilling and Underbalanced Operations Conference & Exhibition, Denver, Colorado, 5–6 April. SPE-143104-MS. https://doi.org/10.2118/143104-MS.
Valliappan, S. and Khalili-Naghadeh, N. 1990. Flow Through Fissured Porous Media With Deformable Matrix. *Int J Numer Methods Eng* **29:** 1079–1094. https://doi.org/10.1002/nme.1620290512.
Ward, C. and Clark, R. 1998. Anatomy of a Ballooning Borehole Using PWD Tool. Presented at the 3rd Workshop, Overpressures in Petroleum Exploration, Pau, France.
Watson, G. N. 1922. *A Treatise on the Theory of Bessel Functions*. New York: Cambridge University Press.
Wilson, R. K. and Aifantis, E. C. 1982. On the Theory of Consolidation With Double Porosity. *Int J Eng Sci*, **20** (9), 1009–1035. https://doi.org/10.1016/0020-7225(82)90036-2.
Xingquan, Z., Yingcao, Z., Xiaoqiang, Z., et al. 2015. Kick Detection and Simulation in Accurate Managed Pressure Drilling. *J Southwest Pet Univ*. **37** (5).
Yuan, Z., Morrell, D., Mayans, A. G. et al. 2016. Differentiate Drilling Fluid Thermal Expansion, Wellbore Ballooning and Real Kick During Flow Check With an Innovative Combination of Transient Simulation and Pumps Off Annular Pressure While Drilling. Presented at the IADC/SPE Drilling Conference and Exhibition, Fort Worth, Texas, 1–3 March. SPE-178835-MS. https://doi.org/10.2118/178835-MS.
Zhang, J., Bai, M., and Roegiers, J. C. 2003. Dual-Porosity Poroelastic Analyses of Wellbore Stability. *Int J Rock Mech Min Sci* **40** (4): 473–483. https://doi.org/10.1016/S1365-1609(03)00019-4.
Zhou, J., Huang, H., and Deo, M. 2015. Modeling the Interaction Between Hydraulic and Natural Fractures Using Dual-Lattice Discrete Element Method. Presented at the 49th U.S. Rock Mechanics/Geomechanics Symposium, San Francisco, California, 28 June–1 July.
Zoback, M. D., Barton, C. A., Brudy, M., et al. 2003. Determination of Stress Orientation and Magnitude in Deep Wells. *Int J Rock Mech Min Sci* **40** (7–8): 1049–1076. https://doi.org/10.1016/j.ijrmms.2003.07.001.

Appendix A—Material Coefficients

The following are the dual-porosity coefficients as defined by Berryman and Wang (1995).

$$B_{u2} = B_2$$

$$B_{u1} = \frac{v_1/K_1}{[v_1(1/K_f + 1/K_1)]}$$

$$\overline{\alpha}_1 = \frac{(1/K - 1/K_{u1})}{B_{u1}K}$$

$$K_{u1} = \left[\frac{1}{K} + \left(\frac{v_1}{K_1}\right)^2 \frac{1}{v_1(1/K_f + 1/K_1)}\right]^{-1}$$

$$\overline{\alpha}_2 = \frac{(1/K - 1/K_{u2})}{B_{u2}K}$$

$$K_{u1} = \left[\frac{1}{K} + \left(\frac{v_2\alpha_2}{K_2}\right)^2 \frac{B_2K_2}{v_2\alpha_2}\right]^{-1}$$

$$M_1 = \frac{B_{u1}K_{u1}}{\overline{\alpha}_1} \text{ and } M_2 = \frac{B_{u2}K_{u2}}{\overline{\alpha}_2}, \qquad \text{(A-1)}$$

where K_f, K_1, and K_2 are the fluid, fractures, and matrix bulk moduli, respectively (in Pa); B_2 and α_2 are the classic Skempton and Biot-Willis coefficients of the porous matrix; and v_1 and v_2 are the fracture and pore-volume fractions, respectively. Finally, the lumped material coefficient reads as

$$L_0 = \frac{2G(1-\nu)}{1-2\nu} + \overline{\alpha}_1^2 M_1 + \overline{\alpha}_2^2 M_2. \qquad \text{(A-2)}$$

Appendix B—Plane-Strain Problem

With reference to Fig. 2, the inclination and azimuth angles are referred to as α and i, respectively, while the in-situ stresses are along the $x'-, y'-,$ and $z'-$ direction. The wellbore coordinate system is instead along x, y, z. For such a case, the borehole is subjected to both normal and shear stresses ($S_x,\ S_y,\ S_z,\ S_{xy},\ S_{xz},\ S_{yz}$), as shown by the stress transformation given by Jaeger et al. (2009). At the far field ($r \to \infty$), assuming an initial virgin pore pressure, p_0, the following state of stress applies:

$$\begin{aligned}
\sigma_x &= -S_x,\\
\sigma_y &= -S_y,\\
\sigma_{xy} &= -S_{xy},\\
\sigma_{zz} &= -\nu(S_x + S_y) - (1-2\nu)(\ \overline{\alpha}_1 +\ \overline{\alpha}_2)p_0,\\
\sigma_{yz} &= \sigma_{xz} = 0.
\end{aligned} \qquad \text{(B-1)}$$

At the borehole ($r = r_w$), after applying a second transformation into cylindrical coordinates,

$$\sigma_r = -S_r H(-t) - p_w H(t),$$
$$\sigma_{r\theta} = -S_{r\theta} H(-t),$$
$$\sigma_{rz} = -S_{rz} H(-t),$$
$$p_1 = p_0 H(-t) + p_w H(t), \quad \text{(B-2)}$$

where $H(t)$ is the Heaviside function and p_w is the wellbore pressure.

Mode 1. This mode involves the application of a hydrostatic far-field stress. As such, neither rotation nor volumetric strain is generated and, consequently, no pore-pressure variation occurs. The boundary conditions at the well are as follows:

$$\sigma_{rr}^{(1)} = (H_0 - p_w)H(t) = [(S_x + S_y)/2 - p_w]H(t),$$
$$\sigma_{r\theta}^{(1)} = 0,$$
$$p_1^{(1)} = p_2^{(1)} = 0. \quad \text{(B-3)}$$

The solution to this mode is purely elastic and was provided long ago by Lamé (Sadd 2009):

$$\sigma_r^{(1)} = (H_0 - p_w)H(t)r_w^2/r^2,$$
$$\sigma_\theta^{(1)} = -(H_0 - p_w)H(t)r_w^2/r^2,$$
$$\sigma_{r\theta}^{(1)} = p_1^{(1)} = p_2^{(1)} = 0. \quad \text{(B-4)}$$

Mode 2. This mode accounts for the dual pressure diffusion resulting from the hydraulic communication between wellbore and fractured formation. The system of equations (Eq. 9) is solved for the following boundary conditions at the well:

$$\sigma_{rr}^{(2)} = \sigma_{r\theta}^{(2)} = 0,$$
$$p_1^{(2)} = -(p_0 - p_w)H(t). \quad \text{(B-5)}$$

The pore pressures decouple from the deformation response because of the infinite extent of the formation (Rice and Cleary 1976). However, the limited fluid discharge in the fractures requires the following additional condition:

$$r \frac{\partial p_1^{(2)}(r,t)}{\partial r}\bigg|_{r=r_D} = 0, \quad \text{(B-6)}$$

where r_D is the damaged radius. The solution is obtained by means of the finite Hankel transform. A detailed derivation for this mode is given in the study by Baldino et al. (2018).

$$p_1^{(2)}(r,t) = p_w + \pi(p_1^0 - p_w)\sum_{n=1}^{\xi_n} \frac{J_1(\xi_n r_D)J_0(\xi_n r_w)U(\xi_n r)e^{-C_{11}^* \xi_n^2 t}}{[J_0^2(\xi_n r_w) - J_1^2(\xi_n r_D)]}. \quad \text{(B-7)}$$

In Eq. B-7, J_ω and Y_ω are the Bessel functions of first and second kind, respectively, of order ω, with ξ_n being the infinite positive roots of the transcendental equation,

$$J_1(\xi_n r_D)Y_0(\xi_n r_w) - Y_1(\xi_n r_D)J_0(\xi_n r_w) = 0. \quad \text{(B-8)}$$

The coefficient C_{11}^* (in m^2/s) is the generalized hydraulic diffusivity (see section Diagnostic Tool Application to Field Data). The solution for the matrix pore pressure, as given in Baldino et al. (2018), is an undrained response, and thus it is omitted here. From Eq. B-7, the stress distribution for this mode can be computed as well (Baldino and Miska 2018).

Mode 3. In contrast to the previous modes, this case is not axially symmetric, and full poroelastic coupling arises. The boundary conditions at the well read as

$$\sigma_r^{(3)} = -D_0 H(t)\cos[2(\theta - \theta_r)],$$
$$\sigma_{r\theta}^{(3)} = D_0 H(t)\sin[2(\theta - \theta_r)],$$
$$p_1^{(3)} = p_2^{(3)} = 0. \quad \text{(B-9)}$$

where θ_r is the angle of rotation between the wellbore axes and the in-situ-stress directions and D_0 is the deviatoric stress. They are defined with the results from Cui et al. (1997),

$$\theta_r = 0.5\tan^{-1}[2S_{xy}/(S_x - S_y)],$$
$$D_0 = \sqrt{[(S_x - S_y)/2]^2 + S_{xy}^2}. \quad \text{(B-10)}$$

The solution for the fracture pore pressure, derived in the Laplace space, is then

$$\overline{p}_1^{(3)} = \frac{D_0}{s}\left\{\frac{M_1(L_0 - \overline{\alpha}_1^2 M_1)}{L_0}[\mathrm{K}_2(\xi)c_1 + \mathrm{I}_2(\xi)c_{12}] + \frac{M_1 G\overline{\alpha}_1}{L_0}\frac{c_2}{r^2}\right\}\cos[2(\theta - \theta_r)]. \quad \text{(B-11)}$$

In Eq. B-11, M_1, and M_2 are the generalized Biot moduli (in Pa) and L_0 is a lumped porelastic coefficient, which are given in Appendix B. The variable s (in s^{-1}) is the Laplace parameter, while $\xi = r\sqrt{s/C_{11}^*}$. Finally, c_1, c_{12}, and c_2 are integration constants to be determined using the boundary conditions given in Eq. B-9. To determine Eq. B-11 in the time domain, numerical inversion is recommended (Stehfest 1970). For more details, please refer to Baldino and Miska (2018) and Meng et al. (2019).

Appendix C—Volume Derivative and Smoothing

The technique to be implemented is proposed by Bourdet et al. (1989), and it is based on the pressure-derivative diagnosis of reservoir response. The analysis makes use of the three-point derivative (Onur and Al-Saddique 1999):

$$\Delta V'(\ln t_i) = -\frac{\ln\left(\frac{t_{i+1}}{t_i}\right)}{\ln\left(\frac{t_{i+1}}{t_{i-1}}\right)\ln\left(\frac{t_i}{t_{i-1}}\right)}\Delta V_{i-1} + \frac{\ln\left(\frac{t_{i+1}t_{i-1}}{t_i^2}\right)}{\ln\left(\frac{t_{i+1}}{t_i}\right)\ln\left(\frac{t_i}{t_{i-1}}\right)}\Delta V_i + \frac{\ln\left(\frac{t_i}{t_{i-1}}\right)}{\ln\left(\frac{t_{i+1}}{t_{i-1}}\right)\ln\left(\frac{t_{i+1}}{t_i}\right)}\Delta V_{i+1}. \quad \text{(C-1)}$$

If the resulting derivative curve shows excessive noise, a smoothing procedure can be applied. This consists of increasing the distance between the middle point and the point on the left and/or on the right, by "jumping" to the previous or subsequent one, as shown in **Fig. C-1.** The differentiation length is defined as L, and it should be expressed on the time axis scale. In light of what was just said, the smoothing consists of increasing L until the pressure-derivative response becomes smooth enough. It is a good practice to always avoid oversmoothing to avoid distortion of the data. It is generally accepted that optimal values of L should be between 0.2 and 0.3. The maximum smoothing length is instead fixed at 0.5. The differentiation interval is based on the following criterion:

$$L = \min(\Delta x_{\text{left}}; \Delta x_{\text{right}}). \quad \text{(C-2)}$$

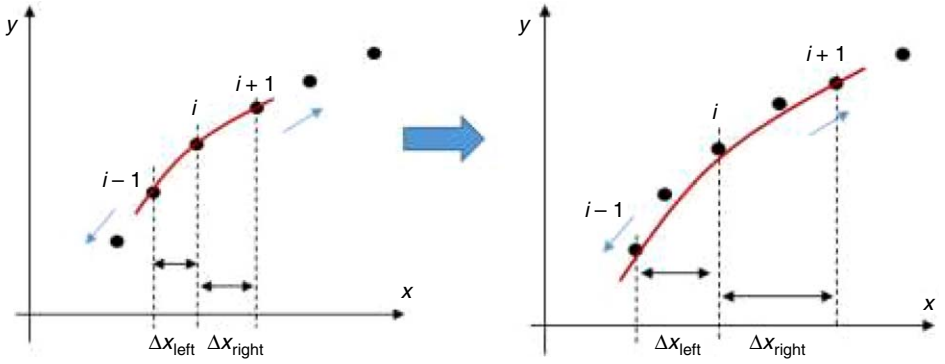

Fig. C-1—Three-point derivative sketch.

For the particular case under study this reduces to

$$L = \min\left[\ln\left(\frac{t_{i+1}}{t_i}\right); \ln\left(\frac{t_i}{t_{i-1}}\right)\right]. \quad \text{(C-3)}$$

Appendix D—Detailed Flow Chart for Protocol Implementation

Fig. D-1 is a detailed flow chart of the steps and calculations necessary to perform the diagnosis of borehole breathing and the subsequent formation characterization.

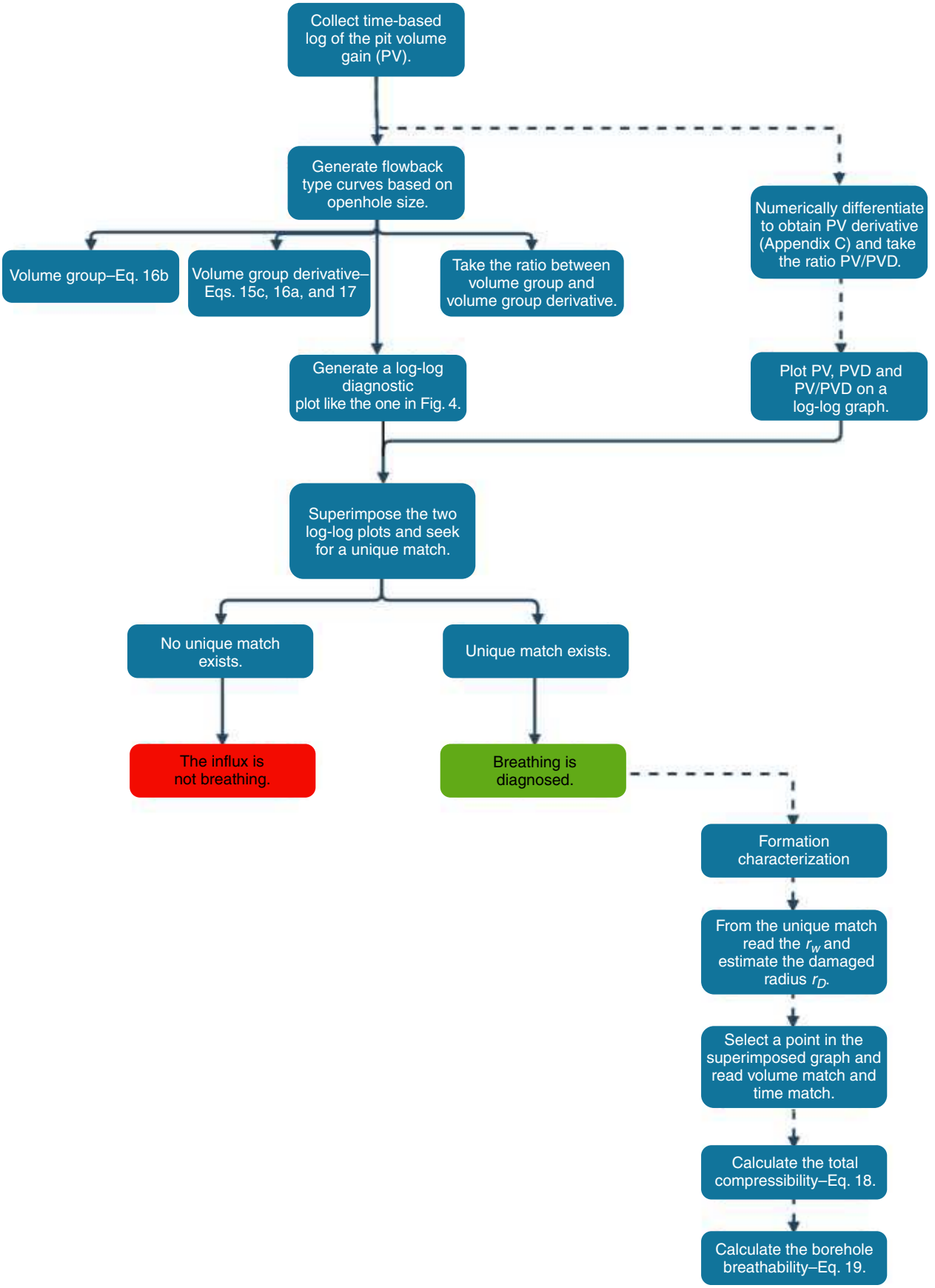

Fig. D-2—Flow chart for diagnostic tool implementation.

SI Metric Conversion Factors

$\text{bbl} \times 1.5898$	$\text{E}-01 = \text{m}^3$
$\text{cp} \times 1.0^*$	$\text{E}-03 = \text{Pa·s}$
$\text{gal/min} \times 6.31$	$\text{E}-05 = \text{m}^3\text{·s}^{-1}$
$\text{psi} \times 6.8947$	$\text{E}+03 = \text{Pa}$
$\text{md} \times 9.8692$	$\text{E}-16 = \text{m}^2$
$\text{lbm/gal} \times 1.1982$	$\text{E}+02 = \text{kg·m}^{-3}$
$\text{in.} \times 2.54^*$	$\text{E}-02 = \text{m}$
$\text{ft} \times 3.048^*$	$\text{E}-01 = \text{m}$

*Conversion factor is exact.

Silvio Baldino is a wells engineer (drilling technology) with Shell in Houston. As a research assistant at TUDRP, he conducted research on well control, geomechanics, and drilling-fluid rheological characterization. Baldino holds BSc and MSc degrees in energy engineering from the Polytechnic University of Milan, Italy, and a PhD degree in petroleum engineering from the University of Tulsa (TU).

Stefan Miska is currently the Jonathan Detwiler Endowed Chair Professor of the McDougall School of Petroleum Engineering and director emeritus of TUDRP at TU. He holds MSc and PhD degrees from the University of Mining and Metallurgy in Cracow, Poland; recently, he was awarded the title of Professor of Technical Sciences by the president of Poland. Miska has been instrumental in the development of research facilities for wellbore hydraulics at simulated downhole conditions. He has made contributions to the development of new buckling concepts and the axial force transfer in extended-reach drilling. Miska is an SPE Distinguished Member and recipient of the 2000 SPE Distinguished Petroleum Engineering Faculty Award, the 2004 SPE Drilling Engineering Award, and the 2018 SPE/AIME Honorary Membership Award.

Evren M. Ozbayoglu is currently the Chapman Endowed Wellspring Associate Professor of Petroleum Engineering at TU, and the director of TUDRP. He holds BSc and MSc degrees from the Middle East Technical University and a PhD degree from TU. Ozbayoglu has participated in several industrial projects on major drilling-engineering topics, including wellbore hydraulics, hole cleaning, tubular mechanics, and fluid rheological characterization. He received the 2012 SPE Outstanding Technical Editor Award for *SPE Journal*, the 2013 SPE Outstanding Technical Editor Award for *SPE Reservoir Evaluation & Engineering*, the 2015 SPE Outstanding Technical Editor Award for *SPE Drilling & Completion*, and the 2013 SPE Regional Distinguished Faculty Award for the Mid-Continent Region.

Jianguo X. Zhang is a rock mechanics/fluids senior specialist with BP at Houston, working on geomechanics, wellbore stability, and drilling fluids. He holds a PhD degree in petroleum engineering from the University of Texas at Austin, and a master's degree in rock mechanics and a bachelor's degree in drilling engineering from the China University of Petroleum.